International Journal of Solids and Structures 50 (2013) 2477–2494

Contents lists available at SciVerse ScienceDirect

International Journal of Solids and Structures

journal homepage: www.elsevier.com/locate/ijsolstr

Coupled mixed-mode cohesive zone modeling of interfacial debonding in simply supported plated beams

Laura De Lorenzis [a,*], Dilum Fernando [b], Jin-Guang Teng [c]

[a] Technische Universität Braunschweig, Institut für Angewandte Mechanik, Bienroder Weg 87, Campus Nord, 38106 Braunschweig, Germany
[b] Institute of Structural Engineering (IBK), Department of Structural, Environmental and Geomatic Engineering (D-BAUG), ETH Zürich, Zürich, Switzerland
[c] Faculty of Construction and Environment, The Hong Kong Polytechnic University, Hong Kong, PR China

ARTICLE INFO

Article history:
Received 1 October 2012
Received in revised form 13 March 2013
Available online 11 April 2013

Keywords:
Cohesive zone modeling
Interfacial stresses
Mixed-mode fracture
Plated beams
Plate end debonding

ABSTRACT

The development of predictive models for plate end debonding failures in beams strengthened with thin soffit plates is a topic of great practical relevance. After the early stress-based formulations, fracture mechanics approaches have become increasingly established. More recently, the cohesive zone (CZ) model has been successfully adopted as a bridge between the stress- and fracture mechanics-based treatments. However, the few studies of this nature propose complex formulations which can only be implemented numerically. To date, the only available analytical solution based on CZ modeling for the prediction of interfacial stresses/debonding in plated beams is limited to the determination of interfacial shear stresses and thus neglects the mixed-mode effects generated by the presence of interfacial normal stresses at the plate end. This paper presents a new analytical formulation based on the CZ modeling approach for the prediction of plate end debonding in plated beams. A key enhancement with respect to the previous solution is the use of a coupled mixed-mode CZ model, which enables a full account of mixed-mode effects at the plate end. The model describes the evolution of the interface after the end of the elastic regime, and predicts the value of the load at incipient debonding. The achievement of a closed-form solution for this quite complex case entails the introduction of a crucial simplifying assumption, as well as the *ad hoc* modeling of an effective cohesive interfacial response. The paper presents the analytical theory and compares its predictions with numerical and experimental results.

1. Introduction

The effectiveness of the plate bonding technique is strongly affected by the performance of the bond between the strengthening plate and the beam substrate, which has thus been extensively researched. In particular, this paper focuses on the so-called plate end debonding mechanism, whereby failure occurs by the formation and rapid growth of an interfacial crack starting from the plate end.

Debonding failures starting from the plate end depend largely on the concentration of interfacial shear and normal stresses between the beam and the bonded plate in the vicinity of the plate end. Thus, many closed-form solutions for these interfacial stresses have been developed, see the review and the original solution by Smith and Teng (2001), and more recent contributions by Deng et al. (2004), De Lorenzis et al. (2006), Stratford and Cadei (2006), Yang et al. (2008) and Zhang and Teng (2010a). In these first-order solutions, both the shear and normal interfacial stresses are assumed to be constant across the thickness of the adhesive layer, which leads to the violation of the shear stress-free condition at the plate ends. The same approach is employed throughout this paper. Higher-order solutions can be found elsewhere (e.g. Rabinovitch and Frostig, 2000; Shen et al., 2001; Yang et al., 2004).

The aforementioned interfacial stress models constitute the basis for plate end debonding models adopting stress-based failure criteria. However, over the past decade, approaches stemming from the framework of linear elastic fracture mechanics (LEFM) have been increasingly adopted (Buyukozturk et al., 2004). In this case, the model assumes a given crack length and estimates the elastic energy release rate. This is then compared to the fracture energy of the relevant material or interface, in order to evaluate the stability of the interfacial crack. Investigations of this type have been presented by Rabinovitch and Frostig (2000), Rabinovitch (2004), Au and Buyukozturk (2006), Yang et al. (2006), Greco et al. (2007), Carpinteri et al. (2009) and De Lorenzis et al. (2010), among others.

Proposed in the 1960s as an alternative to singularity driven fracture mechanics, the cohesive zone (CZ) modeling approach bridges the gap between the stress- and energy-based criteria. Since then, the CZ model has been widely used to simulate fracture under static, dynamic, and cyclic loading conditions for a number

* Corresponding author. Tel.: +49 531391 94350.
E-mail address: l.delorenzis@tu-braunsch weig.de (L. De Lorenzis).

0020-7683/$ - see front matter © 2013 Elsevier Ltd. All rights reserved.
http://dx.doi.org/10.1016/j.ijsolstr.2013.03.035

of materials and bimaterial systems. In a CZ model, the interfacial normal and shear stresses are non-linearly connected to the normal (mode-I) and tangential (mode-II) relative displacements across the interface. As the cohesive interface gradually separates, the magnitude of the interfacial stress at first increases, and then decreases with increasing separation, finally approaching zero. Thus, depending on the level of the interfacial relative displacements, the cohesive interface experiences the entire spectrum of behavior ranging from perfect bonding to complete separation. The main advantage of this approach is the implementation of the crack nucleation and growth mechanisms in a stress analysis procedure.

Surprisingly little attention has been devoted to CZ modeling of plate end debonding in plated beams. As a result, the stress-based and fracture-based approaches referenced earlier have been kept separate in most studies. CZ formulations were adopted by Carpinteri et al. (2007) and Rabinovitch (2008), see also the brief review by De Lorenzis and Zavarise (2009), and more recently by Fernando et al. (2012) and Teng et al. (in press). However, these studies were all based on numerical implementations with the finite element method. With the intention to provide simple predictive tools assisting the development of design rules, De Lorenzis and Zavarise (2009) presented the first closed-form analytical solution for interfacial stresses in plated beams based on the CZ modeling approach. For the sake of simplicity, only the interfacial shear stress was considered, and the interfacial normal stress was neglected. Therefore, this model represents an extension beyond the linear-elastic regime of the early work on plate end interfacial stresses based on the shear-lag assumption. A closed-form expression for the plate end debonding load as a function of material, geometry and cohesive law parameters was derived. A comparison between the predictions of the CZ and the LEFM modeling approaches indicated an asymptotic convergence of the CZ results to the LEFM results when the elastic stiffness and the peak stress of the CZ model tend to infinity, provided that the fracture energy of the interface remains constant. Finally, it was shown that the LEFM predictions can be closely matched to the CZ results in a general case by adopting a fictitious extension of the crack length equal to the size of the softening region of the interface.

In reality, the interfacial layer between the beam and the bonded plate is subjected to a combination of shear and normal stresses, and the debonding process is governed by the combined stress state near the front of the CZ, i.e. at the tip of the debonding crack. Therefore, a more realistic modeling approach calls for the adoption of a mixed-mode CZ law capable of accounting for both stress components and for their combined effect on interfacial damage (De Lorenzis and Zavarise, 2008). While general numerical methods to achieve this are already available, as mentioned in the earlier review, the focus of this work is on analytical tools, which can assist the development of design rules for incorporation into codes of practice.

This paper presents a new analytical formulation based on the CZ modeling approach for the prediction of plate end debonding in plated beams. A key enhancement with respect to the previously proposed solution is the use of a coupled mixed-mode CZ model, which enables a full account of mixed-mode effects at the plate end. The model describes the evolution of the interface following the end of the elastic regime, and predicts the value of the load at incipient debonding. The achievement of a closed-form solution in this quite complex case entails the introduction of a crucial simplifying assumption as well as the *ad hoc* modeling of an effective cohesive interfacial response. The paper presents the analytical theory and compares its predictions with numerical and, albeit indirectly, experimental results. For the purpose of these comparisons, the chosen examples involve steel beams strengthened with carbon FRP (CFRP) laminates, an application which has recently received notable attention (Deng et al., 2004; Deng and Lee, 2007; Colombi and Poggi, 2006; Bocciarelli, 2009; Linghoff et al., 2009; Narmashiri et al., 2012; Teng et al., 2012). Another relevant application is the strengthening of timber beams with steel or FRP plates [e.g. see Dourado et al. (2012)]. In these cases, the cohesive interface physically corresponds to the adhesive layer between the beam and the strengthening plate, and the CZ model thus represents the behavior of this layer.

2. Modeling assumptions

2.1. Problem definition

All the analyses in this paper (Sections 3 and 4) consider a simply supported beam subjected to a point load F at mid-span (Fig. 1). The beam has a cross-section of width b_1 and depth h_1. Although Fig. 1 shows a rectangular cross-section, beams of any cross-sectional shape with a vertical axis of symmetry are considered herein. A thin plate of width b_2, thickness h_2, and length $2l$ is bonded to the soffit of the beam by means of a suitable interface layer. For simplicity, the thickness of this layer, t_a, is not depicted in the figure. Exploiting the symmetric nature of the problem about the mid-span, only half of the beam will be studied. The coordinate x along the beam axis has its origin at the plate end, see Fig. 1.

As the analysis focuses on the plate end debonding process, all the materials involved in the problem except the interface are assumed to have a linear elastic behavior; that is, the non-linearity is concentrated at the interface. The elastic moduli of the beam and the plate materials are respectively denoted as E_1 and E_2.

2.2. CZ model

At the plate–beam interface, both shear and normal stresses arise. For simplicity, this interface can be thought of as a layer of adhesive having constitutive responses under shear and tension given by cohesive laws of a desired shape. Herein, the mode-I and mode-II cohesive laws are assumed to be both of a bilinear shape (see Fig. 2). This shape is able to capture the three characteristic parameters of the interface, i.e. the fracture energy (area underneath the curve), the cohesion strength, and the linear elastic property (slope of the curve in the ascending branch).

For the modelling of mixed-mode conditions, this study adopts the coupled damage CZ model proposed by Camanho et al. (2003). This model requires suitable criteria for both the onset of softening and the propagation of the debonding crack to be established. On this basis, a single damage variable is defined and controls the evolution of the interface under mixed-mode loading conditions. Unlike in the study by Camanho et al. (2003), different interfacial stiffnesses are herein considered for mode-I and mode-II. Only loading behavior is treated, as the primary interest of the present study lies in the computation of the debonding load. The following subsections summarize the basic features of the CZ model, while full details can be be retrieved from Camanho et al. (2003).

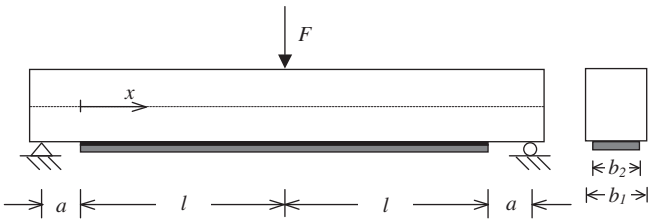

Fig. 1. Simply supported plated beam under a mid-span load.

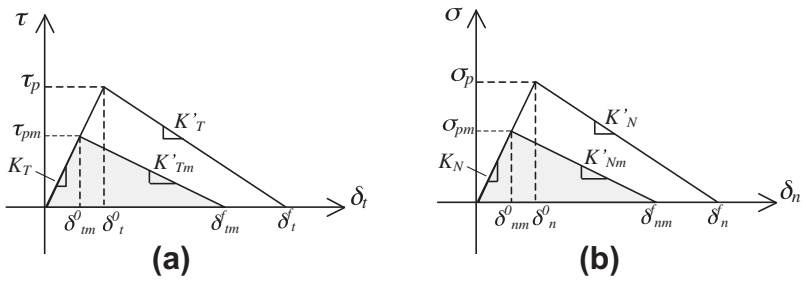

Fig. 2. Interfacial CZ laws. (a) Mode-II. (b) Mode-I.

2.2.1. Basic definitions

Under mixed-mode conditions, coupling is defined through a total mixed-mode relative displacement, δ_m, which is related to the single-mode relative displacements as follows

$$\delta_m = \sqrt{\delta_t^2 + \langle \delta_n \rangle^2} \tag{1}$$

where δ_t and δ_n are respectively the tangential and normal components of the relative displacement across the interface, and the Macaulay operator implies that negative normal relative displacements are assumed not to generate mixed-mode effects. For $\delta_n > 0$, a displacement-based mode-mixity ratio is introduced as follows

$$\gamma = \frac{\delta_t}{\delta_n} \tag{2}$$

By solving the two preceding equations for δ_t and δ_n, the following relationships are obtained

$$\delta_t = \frac{\gamma \delta_m}{\sqrt{1+\gamma^2}} \quad \delta_n = \frac{\delta_m}{\sqrt{1+\gamma^2}} \tag{3}$$

In the model, the coupled mixed-mode damage behavior is described through a single scalar damage variable, d, expressed as a function of the current mixed-mode relative displacement, δ_m, and of the mixed-mode relative displacements at the onset of softening, δ_m^0, and at complete failure, δ_m^f. Therefore, prior to the description of the damage evolution, suitable criteria must be established for the computation of δ_m^0 and δ_m^f.

2.2.2. Criterion for the onset of softening in mixed mode

The shear and normal interfacial stresses before the onset of softening are given by

$$\tau = K_T \delta_t \quad \sigma = K_N \delta_n \tag{4}$$

where K_T and K_N are the interfacial stiffnesses in the tangential and normal directions, respectively (Fig. 2). Under single-mode conditions, the relative displacements at onset of softening are thus given by

$$\delta_t^0 = \frac{\tau_p}{K_T} \quad \delta_n^0 = \frac{\sigma_p}{K_N} \tag{5}$$

where τ_p and σ_p are the peak shear and normal stresses in single mode, respectively (see also Fig. 2).

It is assumed that the onset of softening under mixed-mode conditions occurs when a quadratic stress failure criterion is fulfilled, i.e. when

$$\left(\frac{\tau}{\tau_p}\right)^2 + \left(\frac{\langle \sigma \rangle}{\sigma_p}\right)^2 = 1 \tag{6}$$

where the Macaulay brackets once again imply that normal compressive stresses are not assumed to initiate damage. By substituting Eqs. (1)–(5) into Eq. (6) the following expression is obtained for the total mixed-mode relative displacement at the onset of softening, δ_m^0:

$$\delta_m^0 = \begin{cases} \delta_t^0 \delta_n^0 \sqrt{\frac{1+\gamma^2}{\delta_t^{02} + \gamma^2 \delta_n^{02}}} & \text{if } \delta_n > 0 \\ \delta_t^0 & \text{if } \delta_n \leqslant 0 \end{cases} \tag{7}$$

For $\delta_n > 0$, the tangential and normal relative displacements at the onset of mixed-mode softening, δ_{tm}^0 and δ_{nm}^0, are thus easily obtained through Eq. (3)

$$\delta_{tm}^0 = \frac{\gamma \delta_m^0}{\sqrt{1+\gamma^2}} \quad \delta_{nm}^0 = \frac{\delta_m^0}{\sqrt{1+\gamma^2}} \tag{8}$$

and the combination of Eqs. (7) and (8) yields

$$\delta_{tm}^0 = \delta_t^0 \delta_n^0 \sqrt{\frac{\gamma^2}{\delta_t^{02} + \gamma^2 \delta_n^{02}}} \quad \delta_{nm}^0 = \delta_t^0 \delta_n^0 \sqrt{\frac{1}{\delta_t^{02} + \gamma^2 \delta_n^{02}}} \tag{9}$$

2.2.3. Criterion for propagation of debonding in mixed mode

The energy release rates under mixed-mode critical conditions can be computed as follows (Fig. 2)

$$G_I = \frac{1}{2} K_N \delta_{nm}^0 \delta_{nm}^f \quad G_{II} = \frac{1}{2} K_T \delta_{tm}^0 \delta_{tm}^f \tag{10}$$

where δ_{tm}^f and δ_{nm}^f are the tangential and normal relative displacements at mixed-mode critical conditions. These can be related to the mixed-mode critical total displacement, δ_m^f, through Eq. (3)

$$\delta_{tm}^f = \frac{\gamma \delta_m^f}{\sqrt{1+\gamma^2}} \quad \delta_{nm}^f = \frac{\delta_m^f}{\sqrt{1+\gamma^2}} \tag{11}$$

Propagation of the debonding crack in mixed mode is assumed to occur when the following power-law mixed-mode fracture criterion is fulfilled

$$\left(\frac{G_I}{G_{IC}}\right)^\alpha + \left(\frac{G_{II}}{G_{IIC}}\right)^\alpha = 1 \tag{12}$$

where G_{IC} and G_{IIC} are the mode-I and mode-II fracture energies given by

$$G_{IC} = \frac{1}{2} K_N \delta_n^0 \delta_n^f \quad G_{IIC} = \frac{1}{2} K_T \delta_t^0 \delta_t^f \tag{13}$$

If Eqs. (10) and (11) are substituted into Eq. (12) and with some straightforward manipulations the following expression of δ_m^f is finally obtained

$$\delta_m^f = \frac{2(1+\gamma^2)}{\delta_m^0} \left[\left(\frac{K_N}{G_{IC}}\right)^\alpha + \left(\frac{\gamma^2 K_T}{G_{IIC}}\right)^\alpha \right]^{-1/\alpha} \tag{14}$$

In the following, $\alpha = 1$ is always assumed.

2.2.4. Instantaneous CZ models during softening

An instantaneous state of the interface during mixed-mode loading can be visualized as shown in Fig. 2 (shaded triangle). Due to the mixed-mode effect, the relative tangential and normal displacements at the onset of softening (peak interfacial stress) and at complete debonding (zero interfacial stress) are reduced with respect to the corresponding single-mode values. It is important to note that the shaded bilinear responses are variable in time, i.e., they vary during loading as damage progresses, and in space, i.e., they vary from point to point along the interface due to its variable level of damage. In other words, they are *instantaneous* and *local* CZ laws. This aspect notably complicates the analysis with respect to uncoupled CZ approaches, where the CZ law is known *a priori* and can be easily exploited to write the governing differential equations of the interface in the post-peak state (see De Lorenzis and Zavarise, 2009). For a given instant of time and location along the interface, the slopes of the softening branch of the cohesive laws can be computed as follows (Fig. 2)

$$K'_{Tm} = \frac{K_T \delta^0_{tm}}{\delta^f_{tm} - \delta^0_{tm}} \quad K'_{Nm} = \frac{K_N \delta^0_{nm}}{\delta^f_{nm} - \delta^0_{nm}} \tag{15}$$

Through Eqs. (8) and (11) the following relationship can be obtained:

$$\frac{K'_{Tm}}{K_T} = \frac{K'_{Nm}}{K_N} = \frac{\delta^0_m}{\delta^f_m - \delta^0_m} \tag{16}$$

where δ^0_m and δ^f_m are given by Eqs. (7) and (14) as functions of the mixed-mode ratio γ. The following definition is also introduced

$$r_m = \sqrt{\frac{K'_{Tm}}{K_T}} = \sqrt{\frac{K'_{Nm}}{K_N}} \tag{17}$$

Fig. 3a illustrates sample variations of the above ratios versus γ for the example summarized in Table 1. It emerges clearly that both ratios tend to converge to a constant value provided that the mixed-mode ratio γ is sufficiently large.

The peak values of the instantaneous local cohesive laws are given by

$$\tau_{pm} = K_T \delta^0_{tm} = \tau_p \frac{\gamma \delta^0_n}{\sqrt{\delta^{02}_t + \gamma^2 \delta^{02}_n}} \quad \sigma_{pm} = K_N \delta^0_{nm} = \sigma_p \delta^0_t \sqrt{\frac{1}{\delta^{02}_t + \gamma^2 \delta^{02}_n}} \tag{18}$$

Their normalized values τ_{pm}/τ_p and σ_{pm}/σ_p are plotted versus γ in Fig. 3b. Note that, as $\gamma \to \infty$ (pure mode-II conditions), $\tau_{pm} \to \tau_p$ and $\sigma_{pm} \to 0$.

Table 1
Numerical example (beam S303-L).

Geometry data				
b_2 (mm)	y_1 (mm)	y_2 (mm)	A_1 (mm^2)	A_2 (mm^2)
76.0	63.5	1.5	1602	228
I_1 (mm^4)	I_2 (mm^4)	t_a (mm)	l (mm)	a (mm)
4588602	171	1.0	150	400
Material and interface data				
E_1 (N/mm^2)	τ_p (N/mm^2)	δ^0_t (mm)	δ^f_t (mm)	G_{IIc} (N/mm)
205000	26.73	0.0526	0.1197	1.600
E_2 (N/mm^2)	σ_p (N/mm^2)	δ^0_n (mm)	δ^f_n (mm)	G_{Ic} (N/mm)
212000	29.70	0.0037	0.0044	0.065

2.2.5. Damage evolution

As anticipated, damage evolution will be described through a single scalar damage variable d, defined as follows

$$d = \frac{\delta^f_m (\delta_m - \delta^0_m)}{\delta_m \left(\delta^f_m - \delta^0_m\right)} \tag{19}$$

The interfacial stresses are thus defined as

$$\tau = \begin{cases} K_T \delta_t, & \delta_m \leqslant \delta^0_m \\ (1-d) K_T \delta_t, & \delta^0_m < \delta_m < \delta^f_m \\ 0 & \delta_m \geqslant \delta^f_m \end{cases} \tag{20}$$

$$\sigma = \begin{cases} K_N \delta_n, & \delta_m \leqslant \delta^0_m \\ (1-d) K_N \delta_n, & \delta^0_m < \delta_m < \delta^f_m \\ K_N \langle -\delta_n \rangle & \delta_m \geqslant \delta^f_m \end{cases} \tag{21}$$

2.3. Summary of modeling assumptions

The crucial assumptions adopted in developing the proposed analytical model are summarized below, including assumptions which are discussed in detail later in the paper:

(i) shear and normal interfacial stresses are assumed to be constant across the thickness of the adhesive layer, which leads to a first-order solution, see Section 3.1;
(ii) the interfacial behavior is represented by the coupled mixed-mode CZ law by Camanho et al. (2003), as described in Section 2.2;

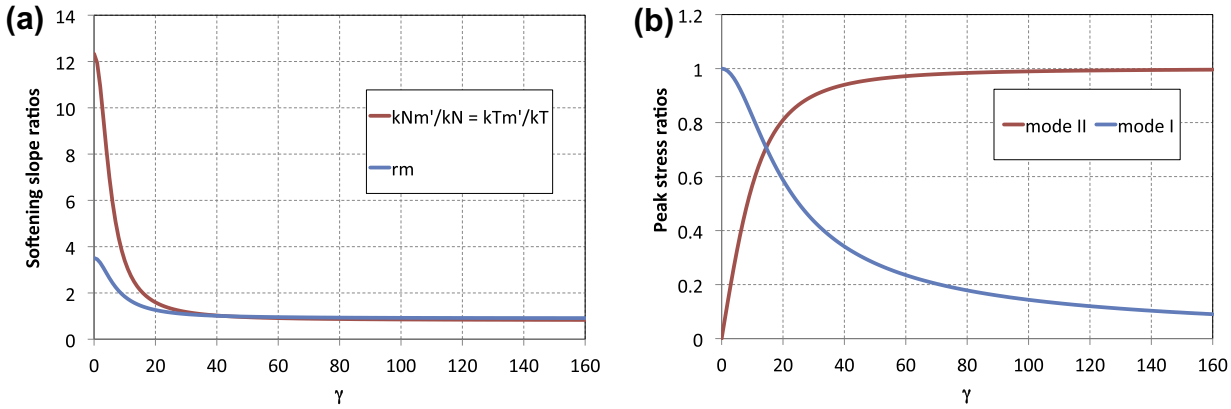

Fig. 3. Instantaneous local softening slope ratios (a) and peak stress ratios (b) as functions of the mixed-mode ratio.

(iii) for the purpose of determining the governing differential equation for the interfacial shear stress, the two adherends (beam and plate) are assumed to have equal curvature, see Section 3.2;
(iv) in order to enable a closed-form solution for the interfacial stresses after the onset of softening accounting for mixed-mode effects, an approximate procedure is introduced where the interfacial relative displacements computed elastically are assumed to be a suitable first-order approximation of the same displacements in the post-elastic range, see Section 4.1.

3. Elastic analysis of the interfacial stresses

This section presents an elastic analysis of the interfacial shear and normal stresses, conducted similarly to Smith and Teng (2001). This analysis serves as the basis for the subsequent examination of the interface in the softening state.

3.1. Equilibrium equations

Fig. 4 illustrates a differential element of beam, adhesive, and bonded plate. The plate is subjected to an axial force N_2, a shear force, V_2, and a bending moment, M_2, whereas the beam is subjected to an axial force, N_1 (taken as positive in compression), a shear force, V_1, and a bending moment, M_1. These are all functions of the coordinate x along the beam axis. The interfacial shear stress, $\tau(x)$, and normal stress, $\sigma(x)$, both act at the interfaces between the beam and the adhesive and between the adhesive and the plate, as well as on the adhesive layer. In this lower-order solution, the two interfacial stresses are both assumed to be uniform across the adhesive thickness.

From Fig. 4, the following equilibrium equations can be easily found for the adherends:

$$\frac{dN_1}{dx} = \tau(x)b_2 \quad \frac{dN_2}{dx} = \tau(x)b_2 \tag{22}$$

$$\frac{dV_1}{dx} = -\sigma(x)b_2 \quad \frac{dV_2}{dx} = \sigma(x)b_2 \tag{23}$$

$$\frac{dM_1}{dx} = V_1(x) - \tau(x)b_2y_1 \quad \frac{dM_2}{dx} = V_2(x) - \tau(x)b_2y_2 \tag{24}$$

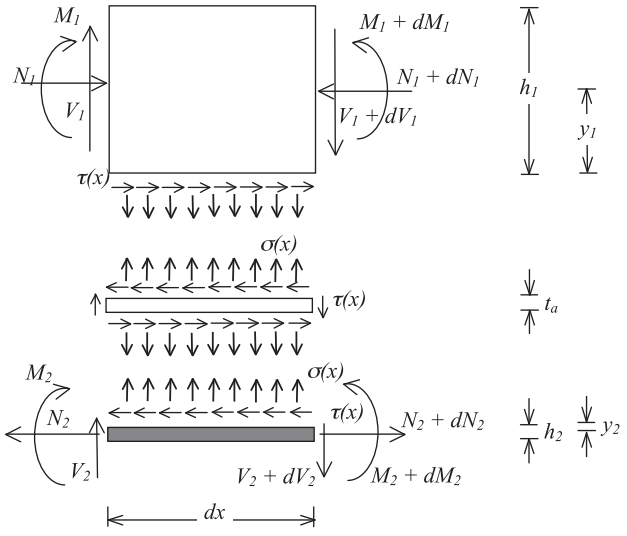

Fig. 4. Differential element of the plated beam.

where y_1 and y_2 are the distances of the bottom fiber of adherend 1 (the beam) and the top fiber of adherend 2 (the plate) from their respective centroids. Moreover, moment equilibrium of the plated beam gives

$$\frac{dM}{dx} = V(x) \tag{25}$$

where $M(x)$ and $V(x)$ are respectively the bending moment and shear force acting on the cross-section of the plated beam at the coordinate x. The moment can be computed as

$$M = M_1 + M_2 + N_1\left(y_1 + \frac{t_a}{2} - y_g\right) + N_2\left(y_2 + \frac{t_a}{2} + y_g\right) \tag{26}$$

with y_g as the distance of the centroid of the plated cross-section from the mid-adhesive axis.

For the simple statically determinate problem in Fig. 1,

$$N(x) = 0 \quad V(x) = \frac{F}{2} \quad M(x) = \frac{F}{2}x \tag{27}$$

where $N(x)$ is the total axial force acting at the cross-section at x. Note that, being from equilibrium $N = N_1 - N_2$, Eq. (27) gives $N_1 = N_2$, hence Eq. (26) becomes

$$M = M_1 + M_2 + N_1(y_1 + y_2 + t_a) \tag{28}$$

3.2. Shear stresses

At small loads, the whole length of the interface is in an elastic state, and experiences no softening or debonding. The interfacial behavior in the tangential direction is thus described by the first branch of the corresponding cohesive law, i.e. by Eq. (20a), where

$$\delta_t = u_2 - u_1 \tag{29}$$

with u_1 and u_2 being the horizontal components of the displacements of, respectively, the bottom fiber of the beam and the top fiber of the plate. Thus Eq. (20a) can also be written as

$$\tau_e(x) = K_T[u_2(x) - u_1(x)] \tag{30}$$

where the subscript "e" has been introduced to refer to the elastic stage. Note that

$$K_T = \frac{G_a}{t_a} \tag{31}$$

where G_a is the shear modulus of the adhesive. The first and second derivatives of Eq. (30) yield

$$\frac{d\tau_e}{dx} = K_T\left[\frac{du_2}{dx} - \frac{du_1}{dx}\right] \tag{32}$$

$$\frac{d^2\tau_e}{dx^2} = K_T\left[\frac{d^2u_2}{dx^2} - \frac{d^2u_1}{dx^2}\right] \tag{33}$$

Denoted as ε_1 and ε_2, respectively, the strains of the bottom fiber of the beam and of the top fiber of the plate, the following relationships hold

$$\varepsilon_1(x) = \frac{du_1}{dx} = \frac{y_1}{E_1I_1}M_1(x) - \frac{1}{E_1A_1}N_1(x) \tag{34}$$

$$\varepsilon_2(x) = \frac{du_2}{dx} = -\frac{y_2}{E_2I_2}M_2(x) + \frac{1}{E_2A_2}N_2(x) \tag{35}$$

If the first derivatives of Eqs. (34) and (35) are substituted into Eq. (33), the following equation results

$$\frac{d^2\tau_e}{dx^2} = K_T\left[-\frac{y_2}{E_2I_2}\frac{dM_2}{dx} + \frac{1}{E_2A_2}\frac{dN_2}{dx} - \frac{y_1}{E_1I_1}\frac{dM_1}{dx} + \frac{1}{E_1A_1}\frac{dN_1}{dx}\right] \tag{36}$$

In the above equation the expressions of $\frac{dN_1}{dx}$ and $\frac{dN_2}{dx}$ from Eq. (22a,b) can now be substituted. For $\frac{dM_1}{dx}$ and $\frac{dM_2}{dx}$, approximate expressions are used hereafter according to the previous work by Smith and Teng (2001). Namely, the two adherends are assumed to have the same curvature, i.e.

$$M_1 = RM_2 \quad R = \frac{E_1 I_1}{E_2 I_2} \tag{37}$$

This basic assumption is of course approximate, as equal curvature would imply perfect bond between the two adherends under bending actions. However, it allows the obtainment of uncoupled differential equations of relatively low order for the interfacial stresses, and its results have been extensively validated by comparison with those from other analytical theories or finite element analyses in a large number of previous works (see e.g. Smith and Teng, 2001; De Lorenzis et al., 2006; Zhang and Teng, 2010a). Eq. (37) combined with Eq. (28) gives

$$M = \frac{R+1}{R} M_1 + N_1(y_1 + y_2 + t_a) \tag{38}$$

By differentiating the above equation and considering Eqs. (25), (22a), and again (37), the following expressions result

$$\frac{dM_1}{dx} = \frac{R}{R+1} V(x) - \frac{R}{R+1} b_2(y_1 + y_2 + t_a)\tau(x) \tag{39}$$

$$\frac{dM_2}{dx} = \frac{1}{R+1} V(x) - \frac{1}{R+1} b_2(y_1 + y_2 + t_a)\tau(x) \tag{40}$$

Substitution of Eqs. (22a,b), (39) and (40) into Eq. (36) yields the following differential equation

$$\frac{d^2\tau_e}{dx^2} - \lambda^2 \tau_e(x) + m_1 \lambda^2 \frac{F}{2} = 0 \tag{41}$$

where

$$\lambda^2 = \bar{K}_T \left[\frac{1}{E_1 A_1} + \frac{1}{E_2 A_2} + \frac{(y_1 + y_2)(y_1 + y_2 + t_a)}{E_1 I_1 + E_2 I_2} \right] \tag{42}$$

and

$$m_1 = \frac{K_T (y_1 + y_2)}{\lambda^2 (E_1 I_1 + E_2 I_2)} \tag{43}$$

with $\bar{K}_T = K_T b_2$. Note that the known expression of $V(x)$ in Eq. (27b) has been introduced.

The general solution of Eq. (41) and its first derivative are given by

$$\tau_e(x) = B_1 cosh\lambda x + B_2 sinh\lambda x + m_1 \frac{F}{2} \tag{44}$$

$$\frac{d\tau_e}{dx} = B_1 \lambda sinh\lambda x + B_2 \lambda cosh\lambda x \tag{45}$$

Two boundary conditions are needed to determine the unknown constants B_1 and B_2. The first condition, stemming from symmetry, is that the shear stress has to be zero on the symmetry axis, i.e.

$$\tau_e(l) = 0 \tag{46}$$

The second one is easily found considering that, for $x = 0$, it is $N_1 = N_2 = 0, M_2 = 0$ and $M_1 = M = Fa/2, a$ being the distance between the support and the plate end (Fig. 1). Therefore, Eqs. (32), (34) and (35) yield

$$\frac{d\tau_e}{dx}(0) = -m_2 \frac{Fa}{2} \tag{47}$$

where

$$m_2 = \frac{K_T y_1}{E_1 I_1} \tag{48}$$

Eqs. (46) and (47) lead to $B_1 = F\tilde{B}_1$ and $B_2 = F\tilde{B}_2$, with

$$\tilde{B}_1 = \frac{1}{2}\left[\frac{m_2 a}{\lambda} tanh\lambda l - \frac{m_1}{cosh\lambda l} \right] \quad \tilde{B}_2 = -\frac{1}{2}\frac{m_2 a}{\lambda} \tag{49}$$

so that Eq. (44) can be normalized with respect to the applied load F as

$$\tilde{\tau}_e(x) = \tilde{B}_1 cosh\lambda x + \tilde{B}_2 sinh\lambda x + \frac{m_1}{2} \tag{50}$$

with $\tau_e(x) = F\tilde{\tau}_e(x)$. The maximum shear stress is reached at the plate end, and can be expressed as follows

$$\tau_{e,max} = F\tilde{\tau}_e(0) = F\left(\tilde{B}_1 + \frac{m_1}{2}\right) \tag{51}$$

The maximum shear relative displacement is also reached at $x = 0$, and is readily obtained as

$$\delta_{te,max} = \delta_{te}(0) = \frac{F}{K_T}\tilde{\tau}_e(0) = \frac{F}{K_T}\left(\tilde{B}_1 + \frac{m_1}{2}\right) \tag{52}$$

where once again the subscript "e" refers to elastic conditions. As a result, τ_e can be finally expressed as

$$\tau_e(x) = \frac{K_T \delta_{te,max}}{\left(\tilde{B}_1 + \frac{m_1}{2}\right)}\left(\tilde{B}_1 cosh\lambda x + \tilde{B}_2 sinh\lambda x + \frac{m_1}{2}\right) \tag{53}$$

The interfacial tangential relative displacement along the interface follows immediately as

$$\delta_{te}(x) = \frac{\delta_{te,max}}{\left(\tilde{B}_1 + \frac{m_1}{2}\right)}\left(\tilde{B}_1 cosh\lambda x + \tilde{B}_2 sinh\lambda x + \frac{m_1}{2}\right) \tag{54}$$

Fig. 5a illustrates the variation of the normalized stress $\tau_e(x)/\tau_p$ along the interface for the numerical example in Table 1. As mentioned earlier, the violation of the shear stress-free condition at the end of the plate is a direct consequence of the assumption of constant shear stress across the thickness of the adhesive layer, and is common to all first-order analytical solutions as well as to numerical models which share this fundamental assumption (Zhang and Teng, 2010b).

3.3. Normal stresses

In the elastic range, the interfacial behavior in the normal direction is described by the first branch of the respective cohesive law, i.e. by Eq. (21a) with

$$\delta_n = v_2 - v_1 \tag{55}$$

v_1 and v_2 being the vertical components of the displacements of, respectively, the bottom fiber of the beam and the top fiber of the plate. Thus Eq. (21a) can also be written as

$$\sigma_e(x) = K_N[v_2(x) - v_1(x)] \tag{56}$$

where once again the subscript "e" refers to the elastic stage. In this case it is

$$K_N = \frac{E_a}{t_a} \tag{57}$$

with E_a as the Young's modulus of the adhesive. Neglecting shear deformations, the following equations hold

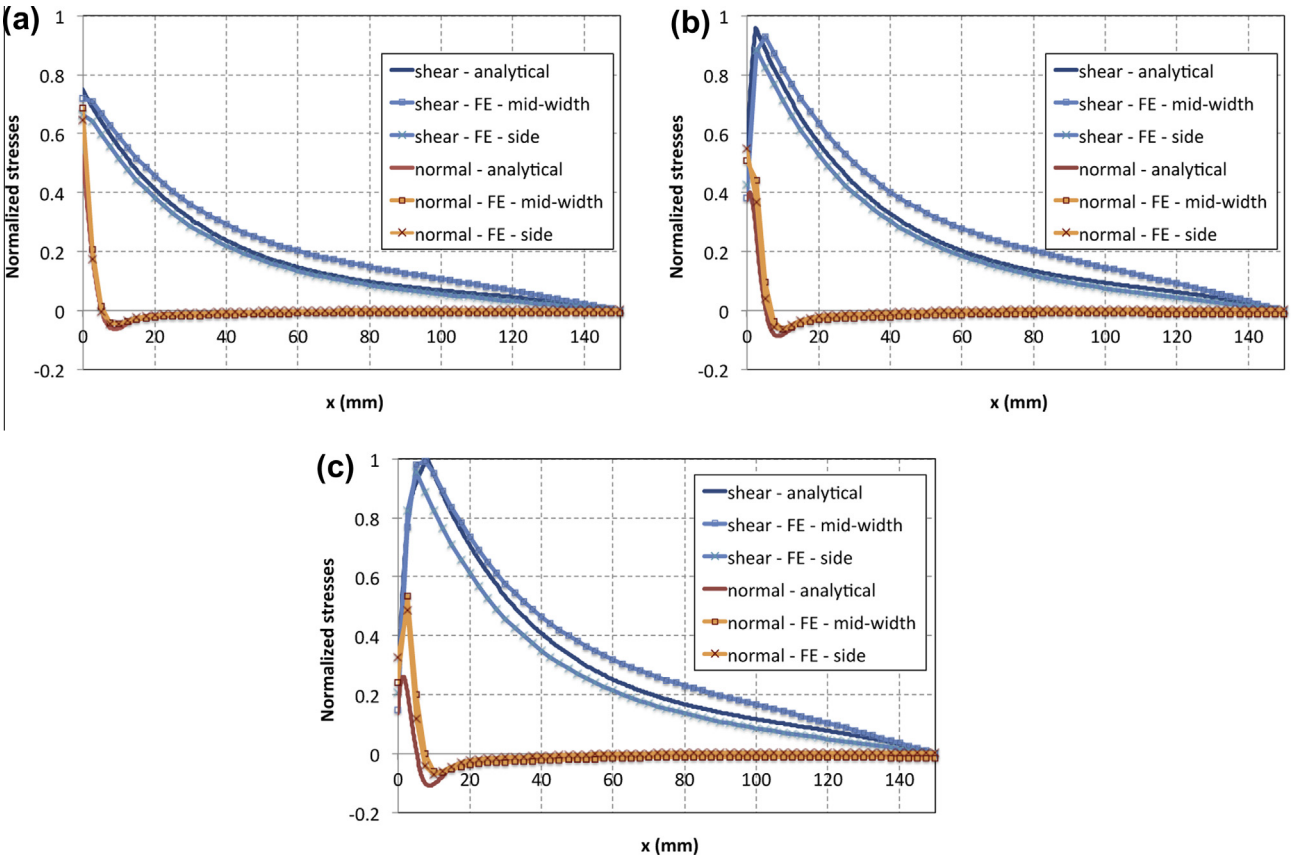

Fig. 5. Normalized interfacial stresses τ/τ_p and σ/σ_p along the plate mid-width from analytical and FE models (beam S303-L). (a) $F = F_1 = 89.5$ kN (elastic stage). (b) $F = F_2 = 121$ kN (E-S stage, $\bar{x} = 2.4$ mm). (c) $F = F_3 = 136.7$ kN (E-S stage, $\bar{x} = 8.4$ mm).

$$\frac{d^2 v_1}{dx^2} = -\frac{1}{E_1 I_1} M_1(x) \quad \frac{d^2 v_2}{dx^2} = -\frac{1}{E_2 I_2} M_2(x) \tag{58}$$

so that the second derivative of Eq. (56) reads

$$\frac{d^2 \sigma_e}{dx^2} = K_N \left[\frac{M_1}{E_1 I_1} - \frac{M_2}{E_2 I_2} \right] \tag{59}$$

Further differentiation of Eq. (58), considering also Eq. (24a,b), leads to

$$\frac{d^3 v_1}{dx^3} = -\frac{1}{E_1 I_1} \frac{dM_1}{dx} = -\frac{1}{E_1 I_1} [V_1(x) - \tau_e(x) b_2 y_1] \tag{60}$$

$$\frac{d^3 v_2}{dx^3} = -\frac{1}{E_2 I_2} \frac{dM_2}{dx} = -\frac{1}{E_2 I_2} [V_2(x) - \tau_e(x) b_2 y_2] \tag{61}$$

hence the third derivative of Eq. (56) becomes

$$\frac{d^3 \sigma_e}{dx^3} = K_N \left\{ \frac{1}{E_1 I_1} [V_1(x) - \tau_e(x) b_2 y_1] - \frac{1}{E_2 I_2} [V_2(x) - \tau_e(x) b_2 y_2] \right\} \tag{62}$$

Finally, due to Eq. (23a,b), the derivatives of Eqs. (60) and (61) can be expressed as

$$\frac{d^4 v_1}{dx^4} = -\frac{1}{E_1 I_1} \left[\frac{dV_1}{dx} - \frac{d\tau_e}{dx} b_2 y_1 \right] = \frac{b_2}{E_1 I_1} \left[\sigma_e(x) + \frac{d\tau_e}{dx} y_1 \right] \tag{63}$$

$$\frac{d^4 v_2}{dx^4} = -\frac{1}{E_2 I_2} \left[\frac{dV_2}{dx} - \frac{d\tau_e}{dx} b_2 y_2 \right] = \frac{b_2}{E_2 I_2} \left[-\sigma_e(x) + \frac{d\tau_e}{dx} y_2 \right] \tag{64}$$

Substitution of Eqs. (63) and (64) into the fourth derivative of Eq. (56) yields

$$\frac{d^4 \sigma_e}{dx^4} + 4\beta^4 \sigma_e(x) = -n_3 \frac{d\tau_e}{dx} \tag{65}$$

with

$$4\beta^4 = \bar{K}_N \left[\frac{1}{E_1 I_1} + \frac{1}{E_2 I_2} \right] \tag{66}$$

$$n_3 = \bar{K}_N \left[\frac{y_1}{E_1 I_1} - \frac{y_2}{E_2 I_2} \right] \tag{67}$$

The general solution of Eq. (65) is given by

$$\sigma_e(x) = e^{-\beta x} [C_1 cos\beta x + C_2 sin\beta x] + e^{\beta x} [C_3 cos\beta x + C_4 sin\beta x] - n_1 \frac{d\tau_e}{dx} \tag{68}$$

where

$$n_1 = \frac{n_3}{4\beta^4} = \frac{y_1 E_2 I_2 - y_2 E_1 I_1}{E_1 I_1 + E_2 I_2} \tag{69}$$

In deriving Eq. (68) it has been assumed that $d^5 \tau_e / dx^5$ can be neglected, as was done by Smith and Teng (2001). By noting that the normal stress is expected to vanish for $x \to \infty$, the constants C_3 and C_4 can be eliminated and the following simpler form of the general solution ensues

$$\sigma_e(x) = e^{-\beta x} [C_1 cos\beta x + C_2 sin\beta x] - n_1 \frac{d\tau_e}{dx} \tag{70}$$

Two boundary conditions are thus needed also in this case to determine C_1 and C_2, which, at $x = 0$, are $M_2 = 0$ and $M_1 = M = Fa/2$. As a result, Eq. (59) gives

$$\frac{d^2\sigma_e}{dx^2}(0) = \frac{K_N}{E_1 I_1}\frac{Fa}{2} \tag{71}$$

Similarly, at $x = 0, V_2 = 0$ and $V_1 = V = F/2$, and Eq. (62) gives

$$\frac{d^3\sigma_e}{dx^3}(0) = \frac{K_N}{E_1 I_1}\frac{F}{2} - n_3\tau_e(0) \tag{72}$$

From Eqs. (71) and (72) the constants C_1 and C_2 are determined as $C_1 = F\tilde{C}_1$ and $C_2 = F\tilde{C}_2$, with

$$\tilde{C}_1 = \frac{K_N}{E_1 I_1}\frac{(1+\beta a)}{4\beta^3} + \frac{n_1\lambda^3}{2\beta^2}\left(\frac{\lambda}{\beta}\tilde{B}_1 + \tilde{B}_2\right) - \frac{n_3}{2\beta^3}\left(\tilde{B}_1 + \frac{m_1}{2}\right) \tag{73}$$

$$\tilde{C}_2 = -\frac{K_N}{E_1 I_1}\frac{a}{4\beta^2} - \frac{n_1\lambda^3}{2\beta^2}\tilde{B}_2 \tag{74}$$

so that Eq. (70) can be normalized with respect to the applied load F as

$$\tilde{\sigma}_e(x) = e^{-\beta x}\left[\tilde{C}_1 cos\beta x + \tilde{C}_2 sin\beta x\right] - n_1\frac{d\tilde{\tau}_e}{dx} \tag{75}$$

with $\sigma_e(x) = F\tilde{\sigma}_e(x)$ and $\frac{d\tilde{\tau}_e}{dx} = \lambda\left(\tilde{B}_1 senh\lambda x + \tilde{B}_2 cosh\lambda x\right)$. The maximum normal tensile stress is reached at the plate end, and can be expressed as follows

$$\sigma_{e,max} = F\tilde{\sigma}_e(0) = F\left(\tilde{C}_1 - n_1\lambda\tilde{B}_2\right) \tag{76}$$

The maximum normal relative displacement, reached at the same location, is

$$\delta_{ne,max} = \frac{F}{K_N}\tilde{\sigma}_e(0) = \frac{F}{K_N}\left(\tilde{C}_1 - n_1\lambda\tilde{B}_2\right) \tag{77}$$

The normal stress σ_e can be finally expressed as

$$\sigma_e(x) = \frac{K_N\delta_{ne,max}}{\left(\tilde{C}_1 - n_1\lambda\tilde{B}_2\right)}\left[e^{-\beta x}\left(\tilde{C}_1 cos\beta x + \tilde{C}_2 sin\beta x\right) - n_1\lambda\left(\tilde{B}_1 senh\lambda x + \tilde{B}_2 cosh\lambda x\right)\right] \tag{78}$$

and the interfacial normal relative displacement along the interface follows as

$$\delta_{ne}(x) = \frac{\delta_{ne,max}}{\left(\tilde{C}_1 - n_1\lambda\tilde{B}_2\right)}\left[e^{-\beta x}\left(\tilde{C}_1 cos\beta x + \tilde{C}_2 sin\beta x\right) - n_1\lambda\left(\tilde{B}_1 senh\lambda x + \tilde{B}_2 cosh\lambda x\right)\right] \tag{79}$$

Fig. 5a illustrates the normalized stress $\sigma_e(x)/\sigma_p$ along the interface for the numerical example in Table 1. Recalling the definition in Eq. (2), the mixed-mode ratio along the interface at the elastic stage for $\delta_{ne} > 0$ is given by

$$\gamma_e(x) = \frac{K_N}{K_T}\frac{\left(\tilde{B}_1 cosh\lambda x + \tilde{B}_2 sinh\lambda x + \frac{m_1}{2}\right)}{\left[e^{-\beta x}\left(\tilde{C}_1 cos\beta x + \tilde{C}_2 sin\beta x\right) - n_1\lambda\left(\tilde{B}_1 senh\lambda x + \tilde{B}_2 cosh\lambda x\right)\right]} \tag{80}$$

and is illustrated in Fig. 6. Note that γ_e tends to infinity (i.e. to pure mode -II conditions) at the location where the interfacial normal stress becomes zero, i.e. at the transition point between tensile (peeling) and compressive normal stresses. Its minimum value, i.e. the most important contribution of mode-I is reached at the plate end, i.e.

$$\gamma_{e,min} = \gamma_e(0) = \frac{K_N}{K_T}\frac{\left(\tilde{B}_1 + \frac{m_1}{2}\right)}{\left[\tilde{C}_1 - n_1\lambda\tilde{B}_2\right]} = \frac{\delta_{te,max}}{\delta_{ne,max}} \tag{81}$$

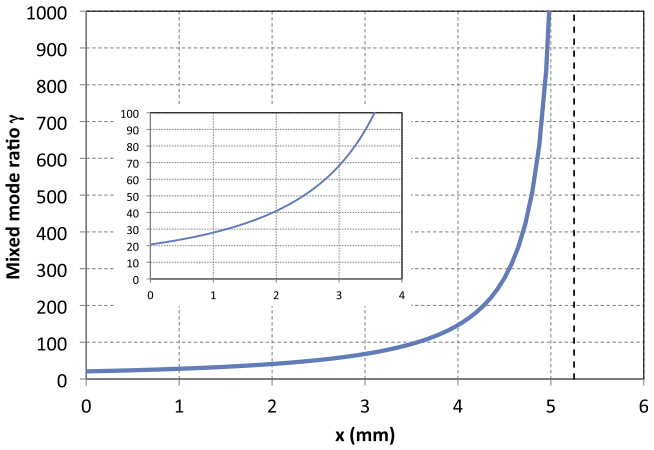

Fig. 6. Mixed-mode ratio along the interface during the elastic stage.

3.4. End of the elastic stage

The interface is entirely elastic until the maximum shear and normal interfacial stresses in Eqs. (51) and (76) fulfil the softening initiation criterion of Eq. (6), from which the load at the onset of softening can be easily computed as follows

$$F_{os} = \left[\left(\frac{\tilde{C}_1 - n_1\lambda\tilde{B}_2}{\sigma_p}\right)^2 + \left(\frac{\tilde{B}_1 + \frac{m_1}{2}}{\tau_p}\right)^2\right]^{-\frac{1}{2}} \tag{82}$$

as a function of geometry and material parameters. Note that the Macaulay brackets in Eq. (6) are not needed in this case, as the maximum normal interfacial stress is always tensile.

4. Interfacial stresses after the onset of softening

4.1. Approximate procedure

Once the interfacial stresses reach the boundary of the elastic domain given by Eq. (6) at $x = 0$, softening of the interface starts at the plate end. As loading progresses, an increasingly long portion of the interface closest to the plate end enters the softening state, while the rest remains in the elastic state. Hereafter, the stage in which the interface is partly elastic and partly softening is indicated as elastic-softening (E-S) stage. The length of the softening zone is denoted as $\bar{x}$.

Along the softening region (i.e. for $0 \leqslant x \leqslant \bar{x}$), the interface undergoes a variable level of damage. Accordingly, the relationship between relative displacements and interfacial stresses varies with x as already noted in Section 2.2.4. This relationship is given by Eqs. (20) and (21), where the damage variable d is defined as in Eq. (19), and depends on the total mixed-mode relative displacement δ_m (given by Eq. (1)) and on the mixed-mode ratio γ. The latter is in turn a function of the unknown relative displacements, see Eq. (2). To sum up, the variation with x of the relation between relative displacements and interfacial stresses is so involved that a closed-form solution of the differential equations governing the interfacial problem in the coupled mixed-mode case appears unfeasible.

As follows, a basic assumption is introduced to facilitate the obtainment of a closed-form solution for the problem. The consequent methodology is termed "the approximate procedure", as opposed to the direct obtainment of a solution to the governing differential equations, which is termed as "the exact procedure" henceforth. The basic assumption and the approximate procedure are outlined as follows.

For $F \leqslant F_{os}$ or, equivalently, for $\delta_{te,max} \leqslant \delta^0_{tm}$ and $\delta_{ne,max} \leqslant \delta^0_{nm}$, the elastic analysis described in Section 3 immediately yields the

correct values of interfacial stresses and relative displacements along the interface. However, for $\delta_{te,max} > \delta^0_{tm}$ and/or $\delta_{ne,max} > \delta^0_{nm}$ the elastic analysis obviously leads to incorrect interfacial *stresses* which overshoot the limits imposed by the cohesive interface laws. Hereafter, it is assumed that the interfacial relative *displacements* resulting from the elastic analysis are a good approximation of the interfacial relative displacements beyond the elastic limit, i.e. in the inelastic (softening) regime. These elastic displacements are thus used as the basis to compute the interfacial stresses using the CZ laws in the appropriate branches (elastic or softening). The adoption of this procedure was inspired by the elastic predictor - plastic corrector scheme regularly used in plasticity numerical settings: there the solution is first let to overshoot the plastic boundary by assuming elastic behavior, and subsequently a correction is applied to the stresses wherever they exceed the imposed limit. In other words, the proposed procedure corresponds to neglecting the effect that the plastic correction to the interfacial stresses bears on the interfacial relative displacements, thus delivering what can be considered a first-order approximation.

On the basis of the preceding simplifying assumption, the approximate procedure consists of the following steps:

- the variable which controls the evolution of the interface is either $\delta_{te,max}$ or $\delta_{ne,max}$. If, say, $\delta_{te,max}$ is chosen, this is gradually increased and the corresponding value of $\delta_{ne,max}$ is computed from Eq. (81). For each value of $\delta_{te,max}$ the length of the softening region, $\bar{x}$, can also be estimated (more details on this are provided later);
- Eqs. (54) and (79), obtained from the elastic analysis described in Section 3, are applied to determine the interfacial relative displacements, i.e. $\delta_t(x) \approx \delta_{te}(x)$ and $\delta_n(x) \approx \delta_{ne}(x)$;
- based on the displacement distributions along the interface, the total mixed-mode relative displacement δ_m (duly accounting for the Macaulay brackets as per Eq. (1)), the mixed-mode ratio γ and consequently the damage variable as well as the interfacial stresses can all be computed as functions of x;
- at this point, the only missing information is the external load that corresponds to the interfacial state of stress. In the elastic stage, the load is obtained from Eq. (52) or equivalently (77). In the E-S stage, the load is computed based on a non-linear relationship between $\bar{x}$ and F which can be obtained as later explained in Section 4.3.2.

Note that the elastic-softening-debonding (E-S-D) stage is not treated herein, as the primary interest lies in the computation of the maximum load sustainable by the interface and this is reached during or at the end of the E-S stage (De Lorenzis and Zavarise, 2009).

4.2. Validation of the approximate procedure for the pure mode-II case

In the Appendix, the use of the approximate procedure is validated for the pure mode-II case, for which a closed-form solution is already available (De Lorenzis and Zavarise, 2009). The Appendix first reviews the latter closed-form solution, which also serves as the basis for the subsequent application of the present approximate procedure to the mixed-mode case. Subsequently, a comparison between interfacial shear stresses evaluated with the exact and the approximate procedures is presented.

Note that the solution illustrated in the Appendix is slightly different from the one first developed in De Lorenzis and Zavarise (2009), as the latter started from equilibrium equations where the presence of interfacial normal stresses as well as shear forces and bending moments in the plate was neglected.

4.3. Application to the mixed-mode case

4.3.1. Computation of the interfacial stresses

Herein, the approximate procedure outlined earlier is applied to the mixed-mode case for the computation of interfacial stresses during the E-S stage. Fig. 5b-c illustrate the results for the numerical example in Table 1. The normalized interfacial stresses $\tau(x)/\tau_p$ and $\sigma(x)/\sigma_p$ are shown along the interface for two different lengths of the softening region $\bar{x}$. The approximate procedure is applied as follows:

- $\delta_{te,max}$ is chosen and the corresponding value of $\delta_{ne,max}$ is computed from Eq. (81). The value of $\bar{x}$ is then computed by substituting Eqs. (53) and (78) into the criterion for the onset of softening Eq. (6), i.e. by solving the implicit non-linear equation

$$\left[\frac{K_T\delta_{te,max}}{\tau_p\left(\tilde{B}_1+\frac{m_1}{2}\right)}\left(\tilde{B}_1 cosh\lambda\bar{x}+\tilde{B}_2 sinh\lambda\bar{x}+\frac{m_1}{2}\right)\right]^2 + \left\{\frac{K_N\delta_{ne,max}}{\sigma_p\left(\tilde{C}_1-n_1\lambda\tilde{B}_2\right)}\left[e^{-\beta\bar{x}}\left(\tilde{C}_1 cos\beta\bar{x}+\tilde{C}_2 sin\beta\bar{x}\right)-n_1\lambda\left(\tilde{B}_1 senh\lambda\bar{x}+\tilde{B}_2 cosh\lambda\bar{x}\right)\right]\right\}^2 = 1 \tag{83}$$

- Eqs. (54) and (79), obtained from the elastic analysis described in Section 3, are applied to determine the interfacial relative displacements, i.e. $\delta_t(x) \approx \delta_{te}(x)$ and $\delta_n(x) \approx \delta_{ne}(x)$;
- based on the displacement distributions along the interface, the total displacement can be evaluated from Eq. (1), the mixed-mode ratio from Eq. (2), and then δ^0_m and δ^f_m from Eqs. (7) and (14), respectively. Finally, the damage variable and consequently the interfacial stresses can be computed from Eqs. (19)–(21) as functions of x.

At the beginning of the E-S stage (Fig. 5b), both the shear and normal interfacial stresses display an abrupt decrease at the plate end. As loading progresses, the peak of the shear stress increases and that of the normal stresses decreases. At a sufficiently advanced stage of loading, the peak of the normal stress further decreases and the peak of the shear stress falls within the region where the normal stress is compressive and damage is only induced by the shear stress, therefore the normalized peak of the shear stress reaches unity (Fig. 5c). At the end of the E-S stage, both interfacial stresses vanish at the plate end. A further increase of $\delta_{te,max}$ would cause the interface to enter the E-S-D stage, whereby the region closest to the plate end will achieve full separation from the beam. As mentioned earlier, this stage is not treated herein.

Fig. 7 illustrates the distributions of the damage variable along the interface corresponding to the stages of loading shown previously. Obviously, the damage variable is only non-zero in the softening portion of the interface. Its trend is close to linearity at the beginning of the E-S stage and becomes increasingly non-linear as loading progresses. The curve corresponding to $F = F_3$ displays an evident change in slope at the location where the normal stress changes sign and damage starts to depend solely on the shear stress.

Finally, Fig. 8 shows the effective CZ laws, i.e. the effective relationships between interfacial stresses and relative displacements along the interface at the different stages of loading. The single-mode laws are also shown for comparison. Fig. 8a shows that the effective cohesive behavior in the tangential direction is obviously linear during the elastic stage ($F = F_1$), is close to being bilinear at

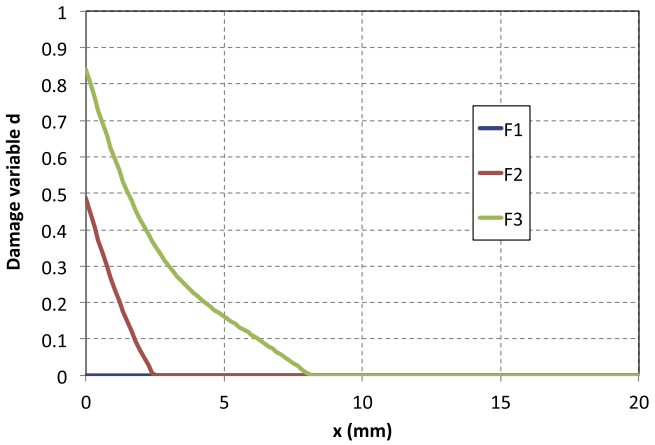

Fig. 7. Damage variable along the interface.

early stages of interfacial softening ($F = F_2$), and becomes increasingly non-linear as loading progresses ($F = F_3$). In all cases, however, the effective relationship follows a large portion of the initial elastic branch, and then a second "effective" softening branch with a distinct decreasing slope. This "effective" softening branch is analyzed in detail in Section 4.3.2. Conversely, the effective cohesive behavior in the normal direction is highly non-linear at all stages of loading (Fig. 8b), showing an almost parabolic shape with a decreasing peak as loading progresses. The information delivered by Fig. 8 is used next to develop a procedure to compute the load levels corresponding to the stages shown in the preceding figures.

4.3.2. Computation of the load level

The only missing piece of information are the levels of load corresponding to the stages illustrated in Figs. 5, 7 and 8. More generally, a procedure is needed to compute the load corresponding to each given value of $\delta_{te,max}$. For this purpose, two key observations can be made:

- if the effective CZ laws in the tangential and normal directions were functions known a priori, they could be used to derive and solve the governing differential equations for the interfacial stresses in the E-S stage, as done in Section A.1 for interfacial shear stresses;
- in Section A.1, the relationship between $\bar{x}$ and the applied load F is found by applying a boundary condition involving the interfacial shear stress. In the mixed-mode case, if the effective CZ law in the tangential direction were a bilinear function known a priori, the same boundary condition would still hold. In other words, Eqs. (A.22) and (A.23) would be still valid under a mixed-mode condition. The presence of interfacial normal stresses would only affect the parameters λ', m_2', and r, which are related to the slope of the softening branch of the tangential cohesive law.

Fig. 9 shows a schematic of the effective tangential CZ law for the mixed-mode case. The softening branch should now be analysed more carefully. This branch is bounded by points A and B, which represent the state of the interface respectively at $x = \bar{x}$ (incipient damage) and $x = 0$ (highest level of damage). Accordingly, their coordinates can be determined as shown and, under the assumption that the softening branch is approximately linear, the slope of segment AB can be easily computed as

$$K'_{Teff} = K_T \frac{1 - [1 - d(0)]\frac{\delta_t(0)}{\delta_t(\bar{x})}}{\frac{\delta_t(0)}{\delta_t(\bar{x})} - 1} \tag{84}$$

In Fig. 10, two dashed lines are also shown, whose slopes are the values of the mixed-mode instantaneous softening slope K'_{Tm} for $x = 0$ and $x = \bar{x}$. They can be considered as a lower and an upper bound of the effective cohesive response, as they stem respectively from the states of the interface at the most damaged ($x = 0$) and at the least damaged ($x = \bar{x}$) locations. The variation of the slope between the lower and the upper bounds is quite small. As visible in Fig. 6, for this example $\gamma(0) = \gamma_{min}$ is slightly larger than 20, which means that the softening slope ratio K'_{Tm}/K_T has almost converged to a constant value (Fig. 3a). However, a larger variation can be observed between the peak stresses, as they achieve convergence for larger values of γ (Fig. 3b).

Fig. 10 illustrates the determination of the effective bilinear tangential cohesive response for the loading stages considered in the preceding subsection. As the load increases, the softening branch of the effective cohesive response deviates increasingly from linearity. However, the linear approximation may still be deemed acceptable even for the last load level, which is close to the end of the E-S stage. Note that the upper bound response for $F = F_3$ collapses to the pure mode-II cohesive law. The reason is that in this case the normal stress for $x = \bar{x}$ is compressive (as already observed earlier from the stress distributions), hence the local response is the same that would be expected for a pure mode-II condition.

Based on the above effective tangential cohesive law, the applied load corresponding to any given softening length $\bar{x}$ can be computed by exploiting earlier results, as follows

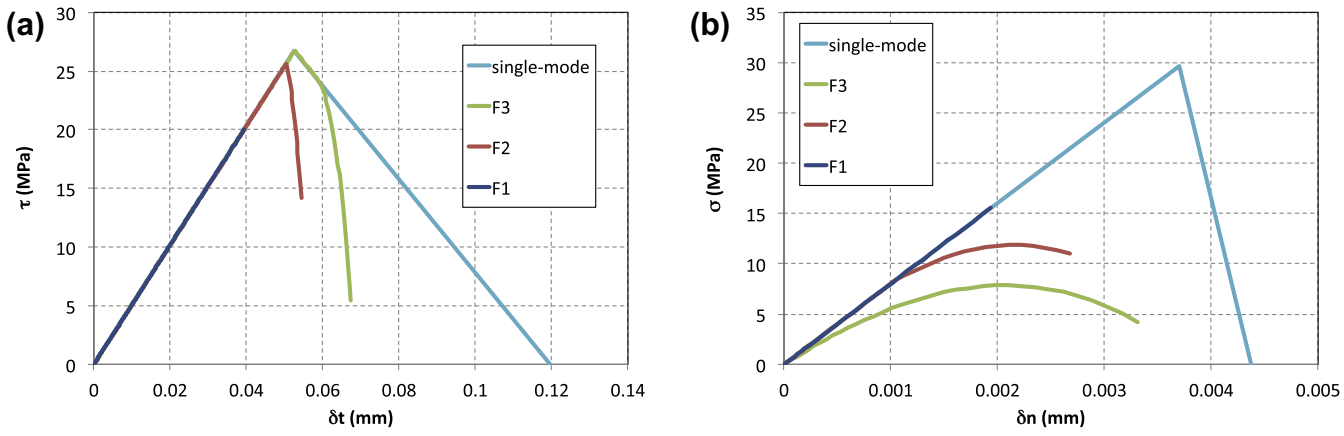

Fig. 8. Effective CZ laws. (a) Mode-II. (b) Mode-I.

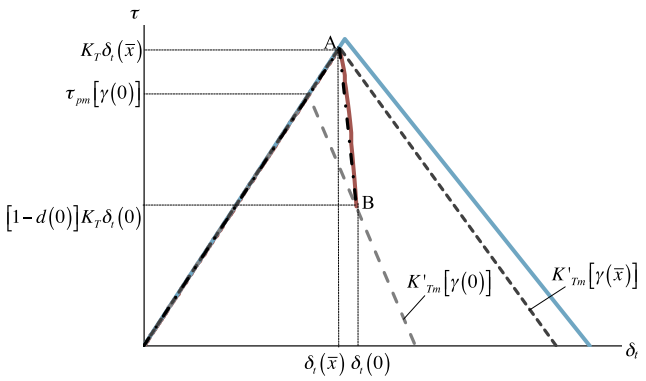

Fig. 9. Effective tangential CZ law under mixed-mode conditions.

$$F = 2\tau_{p,eff} f_{eff}(\bar{x}) \tag{85}$$

where

$$\tau_{p,eff} = K_T \delta_{te}(\bar{x}) \leqslant \tau_p \tag{86}$$

$$f_{eff}(\bar{x}) = \left(tan\lambda'_{eff}\bar{x} + r_{eff} cotgh[\lambda(l-\bar{x})]\right) \Big/ \left(\frac{m_1 sin\lambda'_{eff}\bar{x} + \frac{m'_{2eff}a}{\lambda'_{eff}}}{cos\lambda_{eff}\bar{x}} + m_1 r_{eff}\frac{cosh[\lambda(l-\bar{x})]-1}{sinh[\lambda(l-\bar{x})]}\right) \tag{87}$$

and

$$\lambda'^2_{eff} = \frac{K'_{Teff}}{K_T}\lambda^2 \quad m'_{2eff} = \frac{K'_{Teff} y_1}{E_1 I_1} \quad r_{eff} = \frac{\lambda'_{eff}}{\lambda} = \sqrt{\frac{K'_{Teff}}{K_T}} \tag{88}$$

Fig. 11 illustrates the load computed with the proposed procedure as a function of $\bar{x}$. For comparison, the load computed with the upper and the lower bounds of the cohesive responses, as well as the load predicted based on the mode-II assumption are also shown. The upper bound curve collapses to the mode-II curve as soon as the shear stress peak moves to the region of compressive normal stresses, as in this case the upper-bound local response coincides with that of the single mode-II response. The curve obtained from the proposed approach, based on a mixed-mode coupled CZ model, lies well below the curve obtained without considering the effect of the interfacial normal stress. Moreover, the value of $\bar{x}$ for which the E-S stage ends is much lower in the coupled case than it would be under a pure mode-II condition.

5. Comparison with numerical results

In this section, the predictions of the analytical model are compared with those of three-dimensional finite element (FE) computations implementing the same mixed-mode CZ law.

Fernando (2010) (see also Teng et al., in press) presented detailed FE models of steel beams flexurally-strengthened with CFRP for both intermediate debonding failures and plate end debonding failures, using the same mixed-mode CZ law as employed in this paper. The FE predictions of plate end debonding failures were compared by them with the experimental results of Deng and Lee (2007). An excellent agreement was found, confirming the applicability of this mixed-mode CZ law for predictive purposes in the case under examination.

As the beams tested in Deng and Lee (2007) displayed non-linear material behavior in the steel beam, they were not suitable for direct comparison with the present analytical results. Therefore the strategy adopted in this study was to re-run the FE simulations presented in Fernando (2010) assuming linear material behavior for the steel beam and compare their results with the analytical predictions. In this way, the latter are validated by direct comparison with the FE results for linear steel beam models. In turn, the FE results had been validated by Fernando (2010) by direct comparison with experiments for the non-linear steel beam models. This comparison is deemed to be an indirect but reliable validation of the analytical model with the test results.

Beside enabling this indirect experimental validation, the comparison between analytical and numerical results is needed to evaluate whether the two simplifying assumptions introduced in the analytical model but not shared by the numerical formulation [assumptions (iii) and (iv) given in Section 2.3] yield reasonable results; see Section 5.1.3 for details.

5.1. FE modeling of CFRP-strengthened steel I-beams

5.1.1. Specimen details

Two CFRP-strengthened specimens tested by Deng and Lee (2007) and failed by plate end debonding were selected for comparison with the analytical results. In the original paper by Deng and Lee (2007), these two beams are referred to as specimens S303 and S304, with the last digit referring to the length of the CFRP plate (i.e. S303 had $2l = 300$ mm and S304 had $2l = 400$ mm). Both beams had a total length of 1.2 m, a net span between the supports of 1.1 m, a cross-section of type 127x76UB13, and were subjected to three-point bending as shown in Fig. 1. The beam material was Grade 275 steel, having a nominal yield

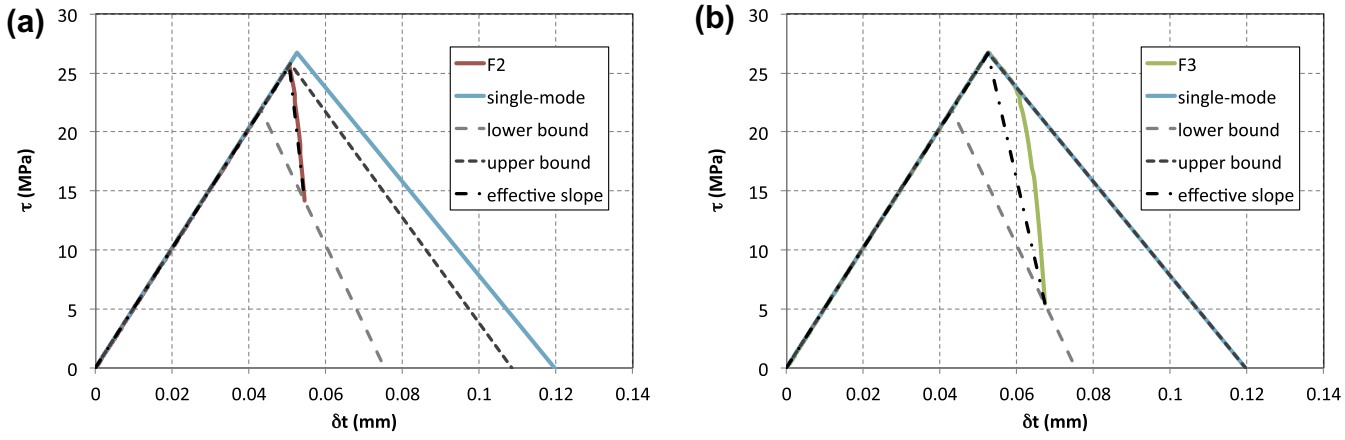

Fig. 10. Evaluation of K'_{Tm}. (a) $F = F_2$. (b) $F = F_3$.

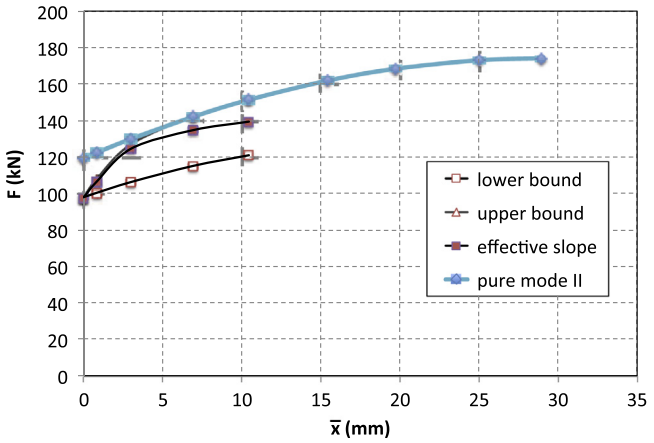

Fig. 11. Evolution of load with the size of softening region.

Table 2
Summary of FE and analytical models.

Specimen/ Model name	Beam material behavior	Intermediate stiffener	$2l$(mm)	a(mm)
S303-L	Linear	none	300	400
S304-L	Linear	none	400	350

strength of 275 MPa and a tensile elastic modulus of 205 GPa. The CFRP plates had a thickness of 3 mm, a width of 76 mm, and an elastic modulus in the fibre direction of 212 GPa. To avoid premature flange buckling and web crushing, two 4 mm thick steel plate stiffeners were welded to each beam at the mid-span, one on each side of the web. Further details can be retrieved from the original paper by Deng and Lee (2007).

5.1.2. FE models

Two different FE models for the two CFRP-strengthened beams were considered (Table 2). The models (termed S303-L and S304-L) assumed linear-elastic steel properties and had no intermediate stiffeners. They were thus suitable for assessment of the analytical model.

The FE model is only briefly outlined herein, as full details can be found in Fernando (2010) and Teng et al. (in press). The model was set up in the general-purpose FE code ABAQUS within a three-dimensional setting, using the shell element S4R with reduced integration for both the steel section and the CFRP plate, and the cohesive interface element COHD8 for the adhesive layer. Based on a mesh convergence study, 2.5 mm × 2.5 mm elements were selected for the steel section and the CFRP plate, while 2.5 mm × 2.5 mm × 1 mm elements (1 mm in the thickness direction) were used to discretize the adhesive layer.

Steel was treated as a linear elastic isotropic material, with an elastic modulus of 205 GPa and a Poisson's ratio of 0.3. The CFRP plate was treated as an orthotropic material. In the fibre direction, the elastic modulus reported by Deng and Lee (2007) was adopted (i.e. $E_2^3 = 212$ GPa based on a nominal thickness of 3 mm). For the elastic modulus in the other two directions, the Poisson's ratios and the shear moduli, the values reported in Deng et al. (2004) were also adopted: $E_2^1 = E_2^2 = 10$ GPa, $v_2^{12} = 0.3$, $v_2^{13} = v_2^{23} = 0.0058$, $G_2^{12} = 3.7$ GPa and $G_2^{13} = G_2^{23} = 26.5$ GPa. The interface element was implemented with the coupled CZ model by Camanho et al. (2003) presented in Section 2.2, with the parameters reported in Table 1. These parameters were derived based on the properties of the adhesive layer as explained in detail by Fernando (2010). Note that similar values of the mode-II fracture energy G_{IIC} were reported by previous researchers studying steel-FRP bonded joints (Xia and Teng, 2005; Akbar et al., 2010).

Note that elastic material properties, geometry data and cohesive properties of the interface for the present FE models are the same as those of the numerical example used in earlier sections and are summarized in Table 1. The only variable data between different models are l and a, see also Table 2.

5.1.3. Basic assumptions of FE vs. analytical models

The FE and the analytical models compared in this section share the first two fundamental assumptions listed in Section 2.3, namely: (i) the shear and normal interfacial stresses are constant across the thickness of the adhesive layer; (ii) the interfacial behavior is represented by the coupled mixed-mode CZ law by Camanho et al. (2003). In particular, due to assumption (i) the FE model also violates the shear stress-free condition at the plate ends.

As listed in Section 2.3 and discussed earlier, two additional simplifying assumptions were introduced into the analytical model in order to achieve a reasonable level of simplicity, namely: (iii) the two adherends have equal curvature; (iv) the elastic interfacial relative displacements are taken as a first-order approximation of the same displacements in the post-elastic regime. Obviously, neither of these two assumptions are present in the numerical model. Therefore, the analytical–numerical comparison not only provides an indirect experimental verification as highlighted earlier but also enables an evaluation of the effects of these two assumptions. A satisfactory correlation between the analytical and the numerical results would imply that assumptions (iii) and (iv) lead to reasonable predictions despite the seemingly crude simplifications they introduce.

5.2. Results

5.2.1. Load vs. mid-span deflection

The load vs mid-span deflection curves for specimens S303-L, S304-L and the unstrengthened steel beam with linear elastic behavior are shown in Fig. 12. Due to the stiffening effect of the CFRP plate, the two strengthened beams showed a slightly higher initial stiffness than the plain beam. As the plate–beam interface entered the softening stage and then the debonding stage, the stiffness gradually decreased and the load–deflection curve converged to that of the plain beam after complete detachment of the plate. The behavior of beam S304-L is similar to that of S303-L. However, as a result of the larger plate length, the initiation of interfacial softening and debonding at the plate end and the corresponding stiffness degradation of the load–displacement curve were delayed. In a real beam, plate end debonding is expected to occur more abruptly and to display a local decrease in load due to dynamic effects. A typical deformed shape from an FE model at plate end debonding failure is given in Fig. 13.

5.2.2. Interfacial stresses

Unlike the analytical solution, the three-dimensional FE model produces interfacial stresses that vary not only along the length but also across the width of the beam. Representative contour plots of the interfacial stresses from the S303-L FE model are shown in Fig. 14 at two load levels within the elastic stage (89.5 kN) and during the E-S stage (136.7 kN). The variation of the interfacial shear stress across the width is visible but limited (Fig. 14a-b). The longitudinal distribution of these stresses maintains a similar pattern across the beam width, but the size of the region featuring significant stresses close to the plate end is slightly larger on the plate mid-width than on the sides of the beam, due to the presence of the web. The normal stress distribution is approximately uniform across the width (Fig. 14c,d). For the purpose of comparing

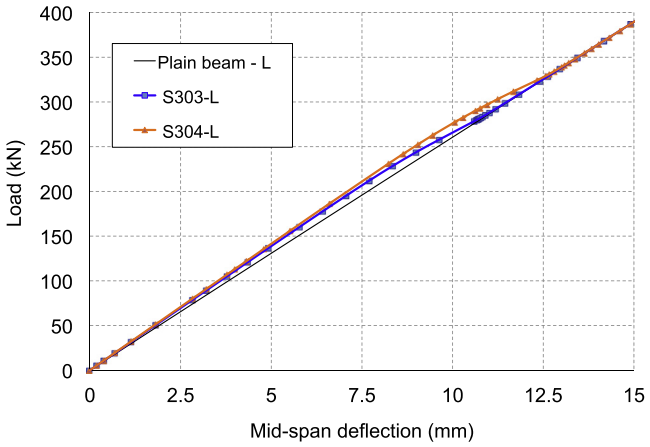

Fig. 12. Load vs. mid-span deflection for plain and CFRP plated steel beams.

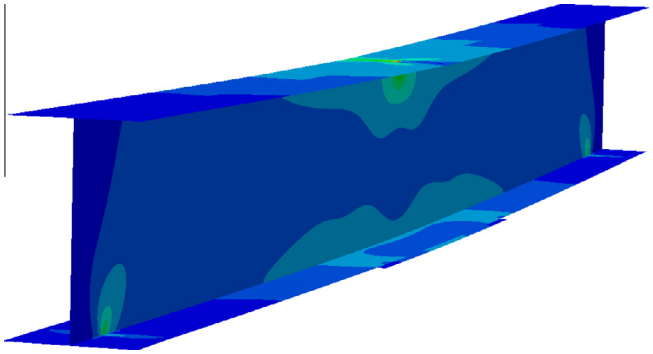

Fig. 13. Typical deformed shape of a steel beam at plate end debonding failure.

the analytical and the FE results, the FE results examined include the interfacial stresses at the mid-width of the beam, and at a distance of 5 mm from the side respectively (the curves are labeled as "mid-width" and "side" in the subsequent figures, respectively).

The interfacial stresses from the FE model and the analytical model are compared in Figs. 5 and 15 for beams S303-L and S304-L, respectively. The loads at the onset of interfacial softening predicted by the analytical model for the two beams are 98.0 kN and 110.7 kN, respectively. The comparison is performed at different load levels within the analytically predicted elastic stage and during the subsequent E-S stage. During the elastic stage, a very close agreement is found between the analytical and the FE results (Figs. 5a and 15a). The analytical distribution of the shear stress is found to lie between the FE curves pertaining to the mid-width and the side of the beam. This indicates that the analytical model succeeds in delivering an approximately average prediction of the interfacial behavior across the width of the beam in this three-dimensional case. As loading progresses and the interface enters the E-S stage, the agreement between analytical and numerical results remains quite satisfactory (5b and 15b). The trend of both sets of data indicates an increase of the maximum shear stress and a simultaneous decrease of the maximum normal stress, as dictated by the mixed-mode failure criterion. At an advanced E-S stage, as noted earlier for the analytical results, the peak of the shear stress moves to within a region where the normal stress is compressive, hence the normalized shear stress peak attains unity. This is predicted by both the analytical and the numerical models (5c and 15c). Despite a certain underestimation of the normal stress, the analytical model thus reproduces quite effectively the numerical interfacial response. During the E-S stage, the analytical shear stress curve continues to be bounded by the numerical curves at the mid-width and the side of the beam.

6. Comparison of different approaches for prediction of plate end debonding

It is useful to compare the outcomes of different approaches in the prediction of the plate end debonding load, i.e. the maximum load sustainable by the interface at the plate end. In Fig. 16, a comparison is presented for a variable mode-II cohesion strength, τ_p, with the mode-II fracture energy G_{IIC} and ductility ratio ($=\delta_t^f/\delta_t^0$) of the interface kept constant. All other parameters are given the values shown in Table 1. The comparison includes predictions of the following methods:

1. a mode-II maximum stress criterion
2. a mode-II LEFM model according to the formulation of De Lorenzis et al. (2010)
3. a mode-II CZ model as per De Lorenzis and Zavarise (2009)
4. a mode-II LEFM model including an effective crack length based on the size of the softening region (De Lorenzis and Zavarise, 2009)
5. a mixed-mode stress criterion based on Eq. (6)
6. a mixed-mode CZ model based on the approximate procedure outlined in this paper.

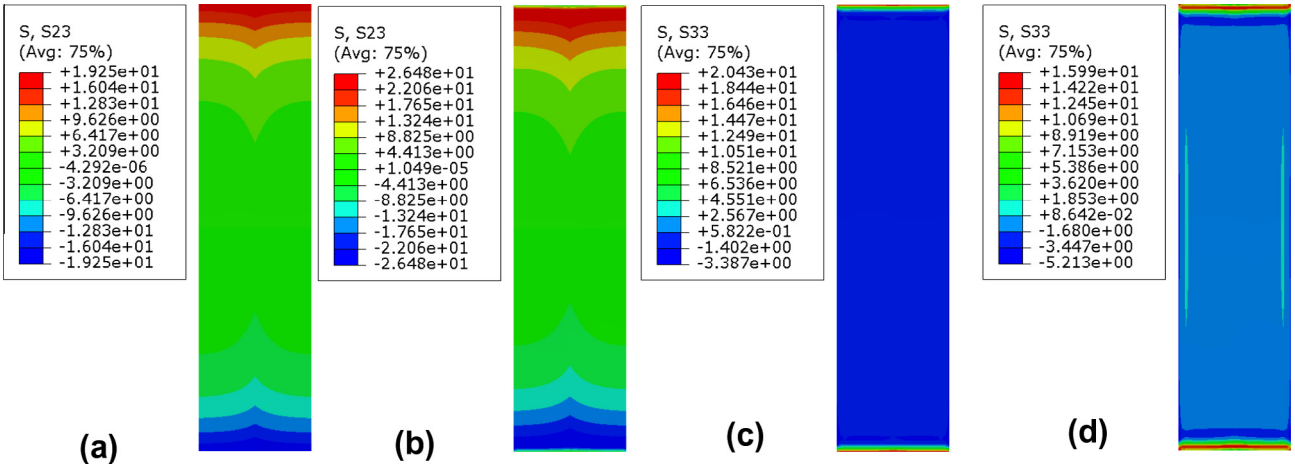

Fig. 14. Interfacial stresses for S303-L. (a) $F = F_1$, shear. (b) $F = F_3$, shear. (c) $F = F_1$, normal. (d) $F = F_3$, normal.

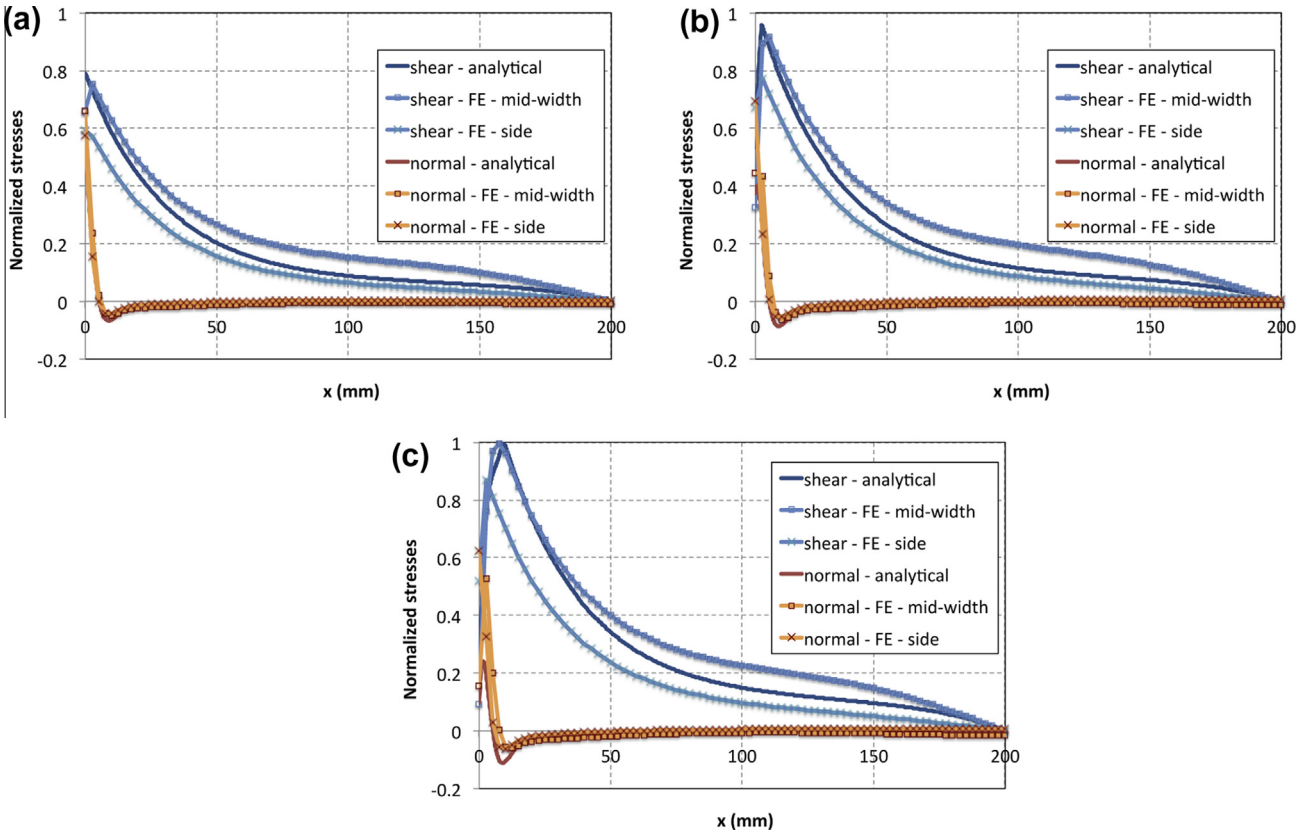

Fig. 15. Normalized interfacial stresses τ/τ_p and σ/σ_p along the plate mid-width from analytical and FE models (beam S304-L). (a) 107 kN (elastic stage). (b) 136.8 kN (E-S stage, $\bar{x} = 2.4$ mm). (c) 156 kN (E-S stage, $\bar{x} = 9.7$ mm).

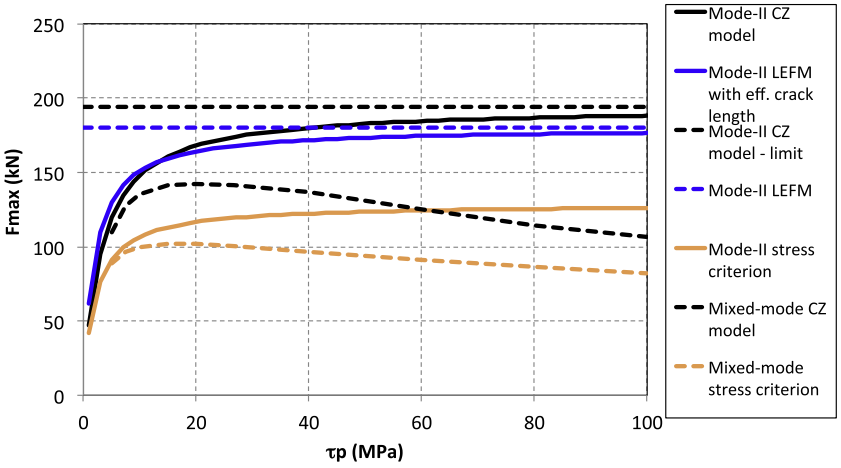

Fig. 16. Plate end debonding load vs. mode-II cohesion strength.

Note that all formulations, except for the last one, deliver closed-form expressions of the plate end debonding load. Several observations can be made:

–stress-based approaches, i.e. methods (1) and (5), are evidently conservative and their use would lead to an uneconomical design of the external strengthening system. Using a mixed-mode criterion obviously leads to a lower predicted debonding load than considering only the mode-II interfacial stresses. Moreover, it interestingly delivers a non-monotonic trend of the debonding load with the mode-II cohesion strength, thus pointing to an "optimal" value of τ_p;

– methods (3) and (4) deliver quite close predictions, which tend to converge towards well-defined limits for very large cohesion strengths. These limits are basically dictated by the LEFM, i.e. by method (2), see De Lorenzis and Zavarise (2009) for a detailed discussion;

–the mixed-mode CZ approach predicts debonding loads that are significantly smaller than those obtained from a pure mode-II CZ model. Therefore, proper consideration of mixed-mode effects is of outmost importance for the safe prediction of plate end debonding. Once again, the non-monotonic trend of the curve seems to indicate that the adhesive layer (or, more generally, the interface) with an "optimal" value of τ_p should be

sought. This is a remarkable result which should be given further attention in future research.

7. A note on the CZ modeling approach

Of the main assumptions made in developing the analytical model and listed in Section 2.3, assumptions (iii) and (iv) have been validated through the analytical–numerical comparison (see Section 5.1.3). The only assumption in need of further discussion is assumption (i), which is shared by the numerical model and therefore cannot be validated by the analytical–numerical comparison. This assumption can be considered to have been indirectly validated by the numerical-experimental comparison carried out by Fernando (2010), which provides an indirect experimental verification for the analytical model (see the introduction to Section 5). However, it is worthwhile to elaborate more on this topic as it is of crucial importance to understand the limitations of the adopted approach.

In reality, significant variations occur in both the shear and the normal interfacial stresses across the thickness of the adhesive layer, as shown by Zhang and Teng (2010b) for the elastic case. Hence, the idealization of this layer as a CZ is obviously an approximation, as the CZ "lumps" all processes taking place within the interface layer of finite thickness into a "macroscopic interfacial law" connecting the relative displacements and the stresses across an "equivalent" interface. This approximation is inherent to the CZ modeling approach in the form adopted in the present study, which is common to a large number of previous studies. The appropriateness of this approach is discussed in more detail below.

The CZ modeling approach is typically applied (most often numerically) in one of two different versions. First, for problems where the debonding crack path is predetermined, cohesive elements are located at this known path. This approach, referred to herein as approach 1, has been extensively used in existing work, for example, in the modeling of delamination in composites where the interfacial debonding is known to take place between the laminae. Although the actual interfacial layer has a finite thickness across which it most often features significant stress variations, for the sake of computational efficiency, its behavior is "lumped" into interface elements, most often with zero thickness and in any case featuring uniform interfacial stresses across the thickness, which can only "macroscopically" represent the actual interfacial behavior. Second, for problems where the geometry of the interface is unknown *a priori*, cohesive interface elements are located between all pairs of adjacent finite elements in a 2D or 3D discretized domain. This approach, referred to herein as approach 2, has been widely used in existing studies to model fracture in quasi-brittle materials such as concretes or ceramics. Here the interfaces between elements are not physical, but rather represent the "constitutive behavior" of a cohesive crack once this forms as a result of stress states in the surrounding elements. These two CZ modeling approaches are quite different in nature, and a CZ model proposed and validated for one approach should only be used in that same approach in order to obtain reliable results.

The coupled mixed-mode CZ law of Camanho et al. (2003) was proposed and validated in the context of approach 1. In the laboratory tests used by these authors for validation, delamination phenomena occurred at finite-thickness interfaces which were likely to be subjected to significant stress variations across the thickness. However, in the numerical setting where Camanho et al. (2003) implemented their mixed-mode CZ law, these finite-thickness interfaces were modeled by "lumping" their behavior into "macroscopic", zero-thickness interface elements situated at the location of the predetermined interface. The analytical model proposed in this paper, by assuming constant interfacial stresses across the thickness of the adhesive layer, implicitly follows approach 1 and consistently adopts the model by Camanho et al. (2003), which was proposed and validated for the same approach. Also consistently, the experimental calibration of the unknown parameters in the CZ model was conducted by Fernando (2010) adopting the same approach. In other words, Camanho's mixed-mode CZ model as calibrated experimentally by Fernando (2010) implicitly considers the effects of interfacial stress variations across the thickness and "lumps" them into a "macroscopic" CZ law.

The above discussions indicate that the use of assumption (i) in the present study is appropriate as it is consistent with the CZ law adopted, as well as with the way the latter was experimentally calibrated. Conversely, it would not be consistent to apply Camanho et al.'s model in combination with a higher order analysis which considers stress variations across the thickness of the adhesive layer, or equivalently with the numerical 2D-2D-2D approach (using the terminology in Zhang and Teng (2010b)), as this would correspond to implementing a mixed-mode law proposed and validated within the context of approach 1 into a model based on approach 2.

Notwithstanding the above explanations, one should be aware that approach 1 does present some significant limitations, which were recently highlighted by De Lorenzis (2012). The "lumping" process referred to above may introduce a dependency of the calibrated parameters of a "macroscopic" model on the boundary conditions of the specific problem under examination. Therefore, e.g., calibration of Camanho et al.'s model based on shear tests of bonded joints (e.g. Yu et al., 2012) and then application of the calibrated parameters to prediction of flexural tests is not guaranteed to yield accurate results. While a deeper investigation into these issues requires much further effort, the numerical and indirect experimental comparisons presented in this paper and in Fernando (2010) provide confidence in the accuracy of the proposed model for the specific case under examination.

8. Conclusions

The coupled mixed-mode CZ model presented in this paper provides a new analytical tool for predicting the plate end debonding load of plated beams, accounting for both shear and normal interfacial stresses at the plate end, as well as their interaction. The model relies upon some important simplifying assumptions, whose validity for a wide range of geometry and material parameters as well as for loading cases different from the one addressed herein should be evaluated with further research. With this further validation and upon verification against more experimental results, the model can be usefully incorporated into existing design guides and codes. Moreover, the approximate procedure devised in this study constitutes a methodology which may be used in combination with different coupled CZ laws to solve mixed-mode debonding problems.

The proposed model, applied in this paper to the analysis of CFRP-strengthened steel beams, may be equally well applied to other cases, such as timber or concrete beams strengthened with steel or FRP laminates, although the CZ laws may be related to different physical phenomena in these cases; for example, in the case of a wet lay-up FRP laminate bonded to a concrete surface, the macroscopic interface in the CZ model physically corresponds to an heterogeneous finite-thickness layer including the superficial concrete and the polymer layer of primer and resin. Despite the general applicability of the presented theory, care should be taken in dealing with quasi-brittle substrate materials such as concrete, where cracking may significantly influence the local distribution of interfacial stresses. The model presented in this paper assumes linear elastic behavior of the strengthened beam, but it could be

generalized in a straightforward manner to cases where significant non-linearities arise in the material behavior, e.g. in the case of steel beams. In cases where the non-linearities are concentrated in small portions of the beam, the proposed model may still provide acceptable predictions of the load at debonding initiation. Consideration of loading and unloading behavior, as well as an extension of the analysis into the debonding stage may also be pursued in further research.

Of the several CZ models incorporating shear and normal effects available in the literature, the one by Camanho et al. (2003) was selected in this study due to its simplicity and availability within a commercial code framework. However, this choice demands a word of caution, as the model was developed to predict delamination in composite materials and is not necessarily suitable for use in different contexts. For the main applications of consideration in this study, i.e. FRP or steel plates bonded to steel, timber or concrete substrates, there is currently no experimental or theoretical basis for the adoption of any given coupled CZ law (De Lorenzis, 2012) although Camanho et al.'s (2003) model is likely to be applicable to steel beams adhesively bonded with an FRP laminate where debonding occurs in the epoxy adhesive layer. Further research should be performed in this area.

Acknowledgement

The first author has received funding for this research from the European Research Council under the European Union's Seventh Framework Programme (FP7/2007–2013)/ ERC Grant agreement n° 279439.

Appendix A. Appendix – Validation of the approximate procedure for the pure mode-II case

A.1. Interfacial shear stresses in the elastic – softening stage

The following analysis considers the same problem as stated in Section 2.1, and extends the elastic analysis of interfacial stresses presented in Section 3 to the E-S stage. This extension is only presented for the interfacial shear stress, in order to obtain a simple closed-form solution similar to that first presented in De Lorenzis and Zavarise (2009). The equilibrium equations derived in Section 3.1 are obviously still valid.

The elastic analysis presented in Section 3 is valid as long as the interfacial stresses fall within the elastic domain, see Eq. (6). If pure mode-II conditions are assumed by neglecting the interfacial normal stress, the end of the elastic stage is simply reached when the interfacial shear stress reaches τ_p at $x = 0$. As loading further progresses, an increasingly long region of the interface close to the plate end enters the softening state, while the rest of the interface remains elastic. At the beginning of this stage, the load increases as the length of the softening zone, $\bar{x}$, increases. As shown by De Lorenzis and Zavarise (2009), the maximum load F_{max} is attained during this stage for a length $\bar{x}_{max}$ of the softening zone. For longer lengths, the load starts decreasing.

In the softening zone, i.e. for $0 \leqslant x \leqslant \bar{x}$, the interfacial behavior is described by the second branch of the tangential cohesive law, assumed to have a bilinear shape as shown in Fig. 2a. Recalling Eq. (29), the analytical expression can thus be written as

$$\tau_s(x) = \tau_0 - K_T'[u_2(x) - u_1(x)] \tag{A.1}$$

where τ_0 and K_T' are respectively the intercept and the slope of the second branch (see Fig. 2a), given by

$$\tau_0 = \frac{\tau_p \delta_t^f}{\delta_t^f - \delta_t^0} \quad K_T' = \frac{\tau_p}{\delta_t^f - \delta_t^0} \tag{A.2}$$

and the subscript s refers to the softening state of the interface. The first and second derivatives of Eq. (A.1) yield

$$\frac{d\tau_s}{dx} = -K_T'\left[\frac{du_2}{dx} - \frac{du_1}{dx}\right] \tag{A.3}$$

$$\frac{d^2\tau_s}{dx^2} = -K_T'\left[\frac{d^2u_2}{dx^2} - \frac{d^2u_1}{dx^2}\right] \tag{A.4}$$

If the first derivatives of Eqs. (34) and (35) are substituted into Eq. (A.4), and by using Eqs. (22a,b) and (39), (40) as for the elastic stage, the following differential equation governing the softening region of the interface is obtained

$$\frac{d^2\tau_s}{dx^2} + \lambda'^2\tau_s(x) - m_1'\lambda'^2\frac{F}{2} = 0 \tag{A.5}$$

where

$$\lambda'^2 = \bar{K}_T'\left[\frac{1}{E_1A_1} + \frac{1}{E_2A_2} + \frac{(y_1+y_2)(y_1+y_2+t_a)}{E_1I_1+E_2I_2}\right] = \frac{\bar{K}_T'}{\bar{K}_T}\lambda^2 \tag{A.6}$$

and

$$m_1' = \frac{K_T'(y_1+y_2)}{\lambda'^2(E_1I_1+E_2I_2)} = m_1 \tag{A.7}$$

The following definition is now introduced:

$$r = \frac{\lambda'}{\lambda} = \sqrt{\frac{K_T'}{K_T}} \tag{A.8}$$

where the second equality stems from Eq. (A.6). Note the analogy with the previous definition by Eq. (17).

The general solution of Eq. (A.5) and its first derivative are given by

$$\tau_s(x) = B_3cos(\lambda' x) + B_4sin(\lambda' x) + m_1\frac{F}{2} \tag{A.9}$$

$$\frac{d\tau_s}{dx} = -B_3\lambda' sin(\lambda' x) + B_4\lambda' cos(\lambda' x) \tag{A.10}$$

As mentioned earlier, Eqs. (A.9) and (A.10) are valid for $0 \leqslant x \leqslant \bar{x}$. In the elastic zone, i.e. for $\bar{x} \leqslant x \leqslant l$, Eqs. (44) and (45) continue to hold. In summary, the interfacial stresses in the E-S stage are given by

$$\tau_s(x) = B_3cos(\lambda' x) + B_4sin(\lambda' x) + m_1\frac{F}{2} \quad 0 \leqslant x \leqslant \bar{x} \tag{A.11}$$

$$\tau_e(x) = B_5cosh(\lambda x) + B_6sinh(\lambda x) + m_1\frac{F}{2} \qquad \bar{x} \leqslant x \leqslant l \tag{A.12}$$

The constants in Eq. (A.12) have been renamed with respect to Eq. (44), as they are different from those determined for the elastic stage. Hence,

$$\frac{d\tau_e}{dx} = B_5\lambda sinh(\lambda x) + B_6\lambda cosh(\lambda x) \tag{A.13}$$

In this case, four boundary conditions have to be imposed to determine the unknown constants B_3, B_4, B_5, and B_6. The first one, stemming from symmetry, is still given by Eq. (46). The second one of the elastic case still holds, i.e., for $x = 0$, it is $N_1 = N_2 = 0$, $M_2 = 0$ and $M_1 = M = Fa/2$. Therefore, in this case Eqs. (A.3), (34) and (35) yield

$$\frac{d\tau_s}{dx}(0) = m_2'\frac{Fa}{2} \tag{A.14}$$

where

$$m_2' = \frac{K_T' y_1}{E_1 I_1} \tag{A.15}$$

The remaining two boundary conditions are found by imposing the continuity of the shear stress at the point of transition between the elastic and the softening regions of the interface:

$$\tau_e(\bar{x}) = \tau_s(\bar{x}) \tag{A.16}$$

and the attainment of the peak shear stress at the same point:

$$\tau_e(\bar{x}) = \tau_p \tag{A.17}$$

Eqs. (46), (A.14), (A.16) and (A.17) give the following values for the constants

$$\begin{aligned} B_3 &= \frac{1}{cos(\lambda'\bar{x})}\left\{\tau_p - \frac{F}{2}\left[m_1 + \frac{m_2' a}{\lambda'} sin\lambda'\bar{x}\right]\right\} \\ B_4 &= \frac{F}{2}\frac{m_2' a}{\lambda'} \\ B_5 &= \frac{1}{sinh[\lambda(l-\bar{x})]}\left\{sinh\lambda l\tau_p + \frac{m_1 F}{2}[sinh\lambda\bar{x} - sinh\lambda l]\right\} \\ B_6 &= -\frac{1}{sinh[\lambda(l-\bar{x})]}\left\{cosh\lambda l\tau_p + \frac{m_1 F}{2}[cosh\lambda\bar{x} - cosh\lambda l]\right\} \end{aligned} \tag{A.18}$$

As the above expressions contain the unknown parameter $\bar{x}$, one more condition is needed for its determination. In order to find it, the derivative of the elastic interfacial shear stress, Eq. (32), and Eqs. (34) and (35) are combined to yield, for $x = \bar{x}$

$$\frac{d\tau_e}{dx}(\bar{x}) = K_T\left[-\frac{y_2}{E_2 I_2}M_2(\bar{x}) + \frac{1}{E_2 A_2}N_2(\bar{x}) - \frac{y_1}{E_1 I_1}M_1(\bar{x}) + \frac{1}{E_1 A_1}N_1(\bar{x})\right] \tag{A.19}$$

Moreover, the derivative of the softening interfacial shear stress given by Eq. (A.3) is combined with Eqs. (34) and (35), to give at $x = \bar{x}$

$$\frac{d\tau_s}{dx}(\bar{x}) = -K_T'\left[-\frac{y_2}{E_2 I_2}M_2(\bar{x}) + \frac{1}{E_2 A_2}N_2(\bar{x}) - \frac{y_1}{E_1 I_1}M_1(\bar{x}) + \frac{1}{E_1 A_1}N_1(\bar{x})\right] \tag{A.20}$$

For $x = \bar{x}, N_1, N_2, M_1$ and M_2 are all continuous. Therefore, a comparison of Eq. (A.19) with Eq. (A.20) yields immediately

$$\frac{d\tau_s}{dx}(\bar{x}) = -\frac{K_T'}{K_T}\frac{d\tau_e}{dx}(\bar{x}) \tag{A.21}$$

The terms $\frac{d\tau_s}{dx}(\bar{x})$ and $\frac{d\tau_e}{dx}(\bar{x})$ of the above equation can be replaced with their expressions obtained from Eqs. (A.10) and (A.13) computed at $x = \bar{x}$. By substituting in the resulting expressions the values of the constants given by Eqs. (A.18), and also recalling Eq. (A.6), the following implicit expression is obtained for $\bar{x}$

$$F = 2\tau_p f(\bar{x}) \tag{A.22}$$

where

$$f(\bar{x}) = (tan\lambda'\bar{x} + rcotgh[\lambda(l-\bar{x})]) \Big/ \left(\frac{m_1 sin\lambda'\bar{x} + \frac{m_2' a}{\lambda'}}{cos\lambda'\bar{x}} + m_1 r\frac{cosh[\lambda(l-\bar{x})] - 1}{sinh[\lambda(l-\bar{x})]}\right) \tag{A.23}$$

Eq. (A.22) provides the relationship between $\bar{x}$ and F at the E-S stage. A simplified expression for $f(\bar{x})$ can be found for cases where $\lambda(l-\bar{x}) > 10$ (which are common for steel- and FRP-plated beams), as follows

$$f(\bar{x}) = (tan\lambda'\bar{x} + r) \Big/ \left(\frac{m_1 sin\lambda'\bar{x} + \frac{m_2' a}{\lambda'}}{cos\lambda'\bar{x}} + m_1 r\right) \tag{A.24}$$

A.2. Ultimate load

The maximum value of applied load sustainable by the interface, F_{max}, is reached during the E-S stage. It can be computed by maximizing $f(\bar{x})$ with respect to $\bar{x}$ in Eqs. (A.23) or (A.24), and substituting the resulting value $\bar{x}_{max}$ into Eq. (A.22). In cases when the simplified Eq. (A.24) holds, it is

$$\bar{x}_{max} = \frac{1}{\lambda'}\arctan\left(\frac{1}{r}\right) = \frac{1}{\lambda'}\arctan\left(\sqrt{\mu_t - 1}\right) \tag{A.25}$$

and consequently

$$\begin{aligned} F_{max} &= 2\tau_p f(\bar{x}_{max}) = 2\tau_p \frac{\sqrt{1+r^2}}{m_1\sqrt{1+r^2} + \frac{m_2' a}{\lambda'}} \\ &= 2\tau_p \frac{\mu_t}{m_1\mu_t + \frac{m_2' a}{\lambda'}\sqrt{\mu_t(\mu_t - 1)}} \end{aligned} \tag{A.26}$$

A.3. Approximate versus exact approaches

The preceding subsection gives a closed-form solution for the interfacial shear stress along the interface during the E-S stage. Hereafter, the approximate procedure outlined in Section 4.1 is applied to this case in order to evaluate the accuracy of the corresponding results.

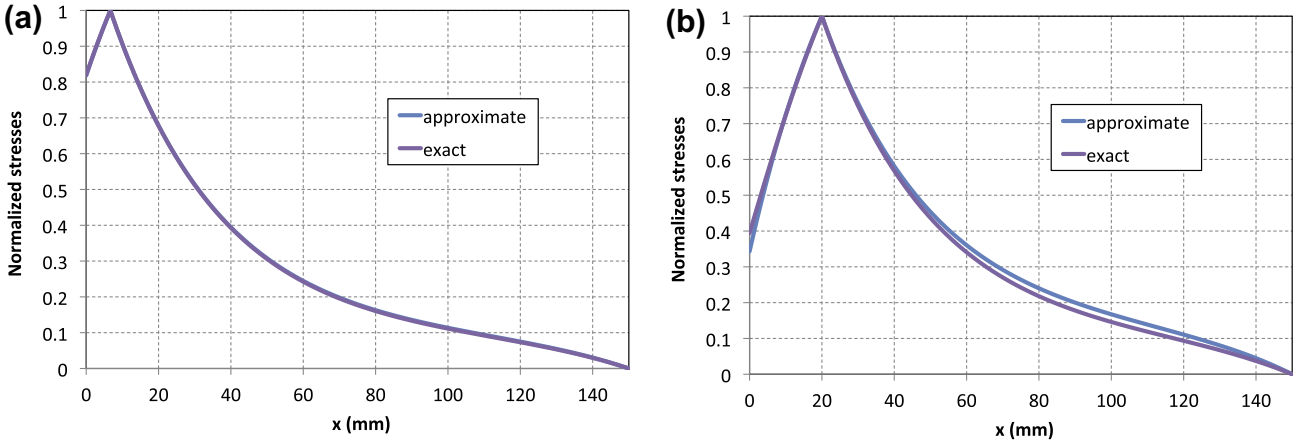

Fig. A.1. Comparison between approximate and exact approaches for the mode-II case. (a) $\bar{x} = 7.13$ mm, $F = 142.7$ kN. (b) $\bar{x} = 20.0$ mm, $F = 168.8$ kN.

Fig. A.1 illustrates the comparison between the results of the exact and the approximate procedures for the numerical example in Table 1. The normalized interfacial shear stress $\tau(x)/\tau_p$ is shown along the interface for two different lengths of the softening region $\bar{x}$. For each value of $\bar{x}$, the exact curve is obtained by computing the unknown constants from Eq. (A.18) and subsequently the shear stress from Eqs. (A.11) and (A.12). The approximate procedure is applied as follows:

- the value of $\delta_{te,max}$ corresponding to the given value of $\bar{x}$ is computed from Eq. (53), considering that $\delta_{te,max}$ is the value of tangential relative displacement at the plate end for which the shear stress at $x = \bar{x}$ would be equal to τ_p

$$\delta_{te,max} = \frac{\tau_p}{K_T} \frac{\left(\tilde{B}_1 + \frac{m_1}{2}\right)}{\left(\tilde{B}_1 cosh\lambda\bar{x} + \tilde{B}_2 sinh\lambda\bar{x} + \frac{m_1}{2}\right)} \tag{A.27}$$

- the elastic tangential relative displacements are computed from Eq. (54). Obviously, the elastic interfacial shear stresses corresponding to these displacements would be larger than τ_p for $0 \leqslant x < \hat{x}$, hence they would overshoot the limit of the elastic range. Based on the main assumption of the approximate procedure, the tangential relative displacements are approximated by the elastic values, i.e. $\delta_t(x) \approx \delta_{te}(x)$;
- the interfacial shear stresses are obtained from $\delta_t(x)$ using the bilinear CZ law in Fig. 2a.

The comparison in Fig. A.1 shows that the difference between the interfacial shear stress values obtained with the two different procedures tends to increase with the length of the softening region, but always remains negligibly small for practical purposes. Note that in both cases the load corresponding to each value of $\bar{x}$ is given by Eq. (A.22).

References

Akbar, I., Oehlers, D.J., Mohamed-Ali, M.S., 2010. Derivation of the bond-slip characteristics for FRP plated steel members. Journal of Constructional Steel Research 66 (8–9), 1047–1056.

Au, C., Buyukozturk, O., 2006. Debonding of FRP plated concrete: a tri-layer fracture treatment. Engineering Fracture Mechanics 73 (3), 348–365.

Bocciarelli, M., 2009. Response of statically determined steel beams reinforced by CFRP plates in the elastic-plastic regime. Engineering Structures 31, 956–967.

Buyukozturk, O., Gunes, O., Karaca, E., 2004. Progress on understanding debonding problems in reinforced concrete and steel members strengthened using FRP composites. Construction and Building Materials 18, 9–19.

Camanho, P.P., Davila, C.G., De Moura, M.F., 2003. Numerical simulation of mixed-mode progressive delamination in composite materials. Journal of Composite Materials 37 (16), 1415–1438.

Carpinteri, A., Lacidogna, G., Paggi, M., 2007. Acoustic emission monitoring and numerical modelling of FRP delamination in RC beams with non-rectangular cross-section. Materials and Structures 40, 553–566.

Carpinteri, A., Cornetti, P., Pugno, N., 2009. Edge debonding in FRP strengthened beams: Stress versus energy failure criteria. Engineering Structures 31, 2436–2447.

Colombi, P., Poggi, C., 2006. An experimental, analytical and numerical study of the static behavior of steel beams reinforced by pultruded CFRP strips. Composites Part B 37, 6473.

De Lorenzis, L., 2012. Some recent results and open issues on interface modeling in civil engineering structures. Materials and Structures 45 (4), 477–503.

De Lorenzis, L., Paggi, M., Carpinteri, A., Zavarise, G., 2010. Linear elastic fracture mechanics approach to plate end debonding in rectilinear and curved plated beams. Advances in Structural Engineering 13 (5), 875–889.

De Lorenzis, L., Teng, J.G., Zhang, L., 2006. Elastic interfacial stresses in curved members bonded with a thin plate. International Journal of Solids and Structures 43 (25–26), 7501–7517.

De Lorenzis, L., Zavarise, G., 2008. Modeling of mixed-mode debonding in the peel test applied to superficial reinforcements. International Journal of Solids and Structures 45, 5419–5436.

De Lorenzis, L., Zavarise, G., 2009. Cohesive zone modelling of interfacial stresses in plated beams. International Journal of Solids and Structures 46 (24), 4181–4191.

Deng, J., Lee, M.M.K., Moy, S.S.J., 2004. Stress analysis of steel beams reinforced with a bonded CFRP plate. Composite Structures 65 (2), 205–215.

Deng, J., Lee, M.M.K., 2007. Behaviour under static loading of metallic beams reinforced with a bonded CFRP plate. Composite Structures 78 (2), 232–242.

Dourado, N., Pereira, F.A.M., de Moura, M.F.S.F., Morais, J.J.L., 2012. Repairing wood beams under bending using carbon-epoxy composites. Engineering Structures 34, 342–350.

Fernando, D., 2010. Bond behavior and debonding failures in CFRP-strengthened steel members. PhD dissertation, Hong Kong Polytechnic University, Hong Kong, China.

Fernando, D., Yu, T., Teng, J.G., 2012. Finite element analysis of debonding failures in CFRP-strengthened rectangular steel tubes subjected to an end bearing load. In: Proceedings, Sixth International Conference on FRP Composites in Civil Engineering, 13–15 June, Rome, Italy.

Greco, F., Lonetti, P., Blasi, N., 2007. An analytical investigation of debonding problems in beams strengthened using composite plates. Engineering Fracture Mechanics 74 (3), 346–372.

Linghoff, D., Haghani, R., Al-Emrani, M., 2009. Carbon-fibre composites for strengthening steel structures. Thin-walled Structures 47, 1048–1058.

Narmashiri, K., Sulong, N.H.R., Jumaat, M.Z., 2012. Failure analysis and structural behaviour of CFRP strengthened steel I-beams. Construction and building materials 30, 1–9.

Rabinovitch, O., 2004. Fracture-mechanics failure criteria for RC beams strengthened with FRP strips - a simplified approach. Composite Structures 64, 479–492.

Rabinovitch, O., 2008. Debonding analysis of fiber-reinforced-polymer strengthened beams: cohesive zone modeling versus a linear elastic fracture mechanics approach. Engineering Fracture Mechanics 75, 2842–2859.

Rabinovitch, O., Frostig, Y., 2000. Closed-form high-order analysis of RC beams strengthened with FRP strips. Journal of Composites for Construction 4, 65–74.

Shen, H.S., Teng, J.G., Yang, J., 2001. Interfacial stresses in beams and slabs bonded with thin plates. Journal of Engineering Mechanics 127 (4), 399–406.

Smith, S.T., Teng, J.G., 2001. Interfacial stresses in plated beams. Engineering Structures 23, 857–871.

Stratford, T., Cadei, J., 2006. Elastic analysis of adhesion stresses for the design of a strengthening plate bonded to a beam. Construction and Building Materials 20 (1-2), 34–45.

Teng, J.G., Yu, T., Fernando, D., 2012. Strengthening of steel structures with fiber-reinforced polymer composites. Journal of Constructional Steel Research 78, 131–143.

Teng, J.G., Fernando, D., Yu, T., in press. Finite element modelling of debonding failures in steel beams flexurally strengthened with CFRP laminates.

Xia, S.H., Teng, J.G., 2005. Behavior of FRP-to-steel bond joints. In: International Symposium on Bond Behaviour of FRP in Structures (BBFS 2005), Hong Kong, China.

Yang, J., Teng, J.G., Chen, J.F., 2004. Interfacial stresses in soffit-plated reinforced concrete beams. Proceedings of the Institution of Civil Engineering, Structures and Buildings 157, 77–89.

Yang, J., Ye, J., Niu, Z., 2008. Simplified solutions for the stress transfer in concrete beams bonded with FRP plates. Engineering Structures 30, 533–545.

Yang, Q.S., Peng, X.R., Kwan, A.K.H., 2006. Strain energy release rate for interfacial cracks in hybrid beams. Mechanics Research Communications 33 (6), 796–803.

Yu, T., Fernando, D., Teng, J.G., Zhao, X.L., 2012. Experimental study on CFRP-to-steel bonded interfaces. Composites Part B: Engineering 43 (5), 2279–2289.

Zhang, L., Teng, J.G., 2010a. Simple general solution for interfacial stresses in plated beams. Journal of Composites for Construction 14 (4), 434–442.

Zhang, L., Teng, J.G., 2010b. Finite element prediction of interfacial stresses in structural members bonded with a thin plate. Engineering Structures 32 (2), 459–471.